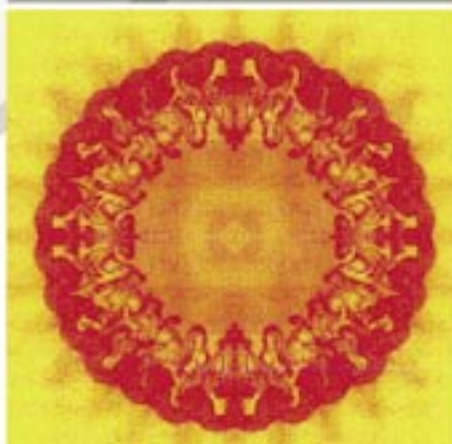
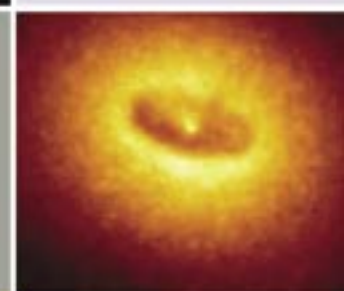
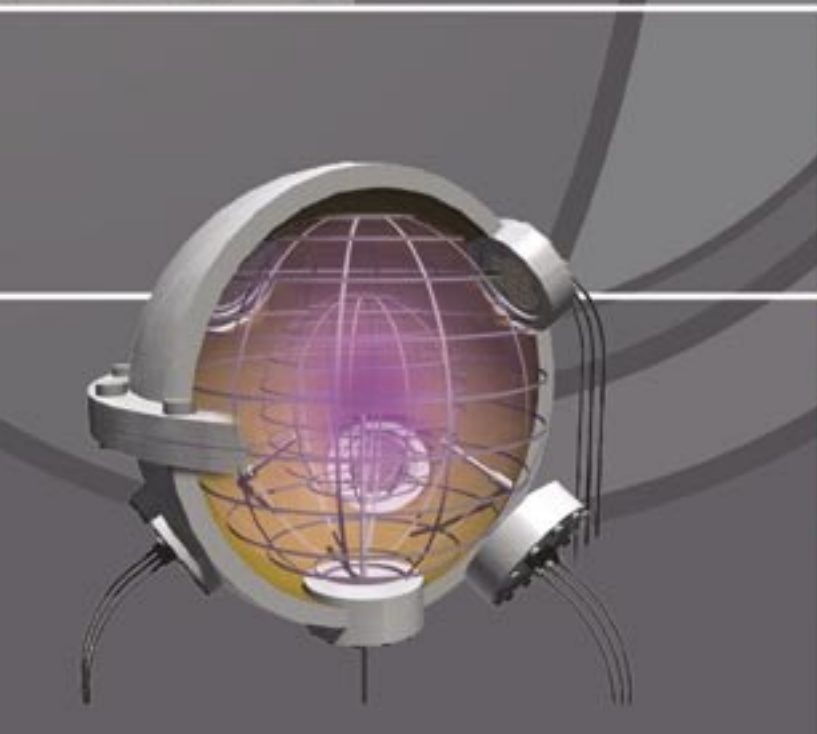
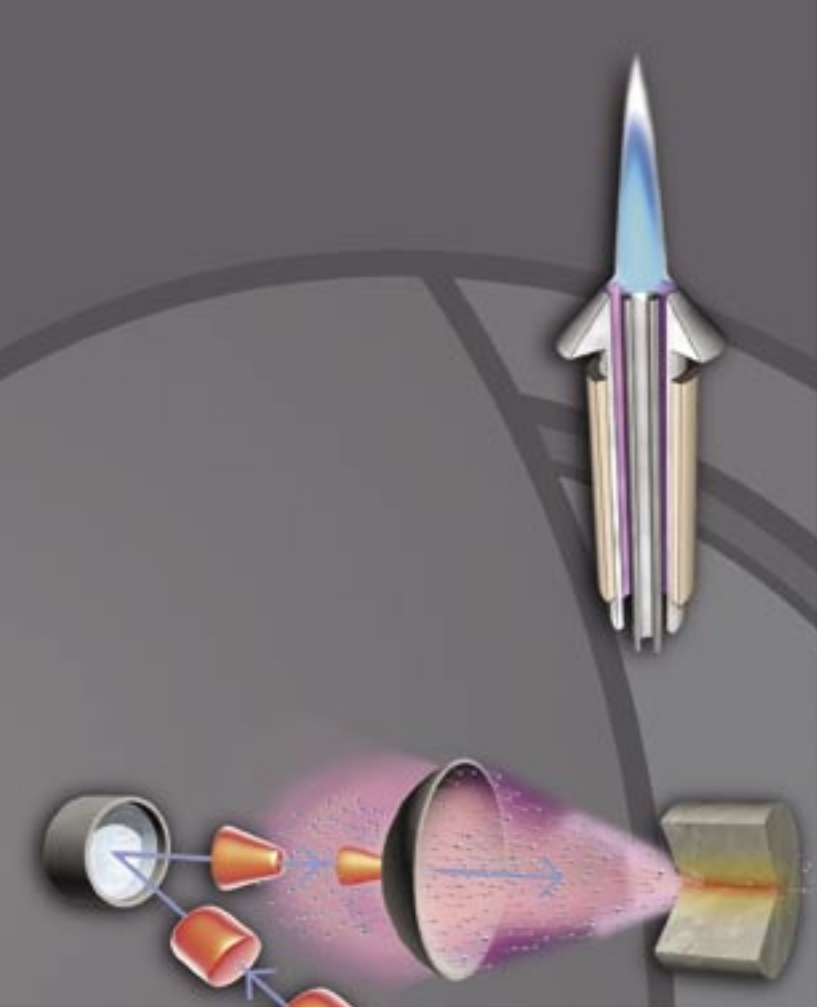
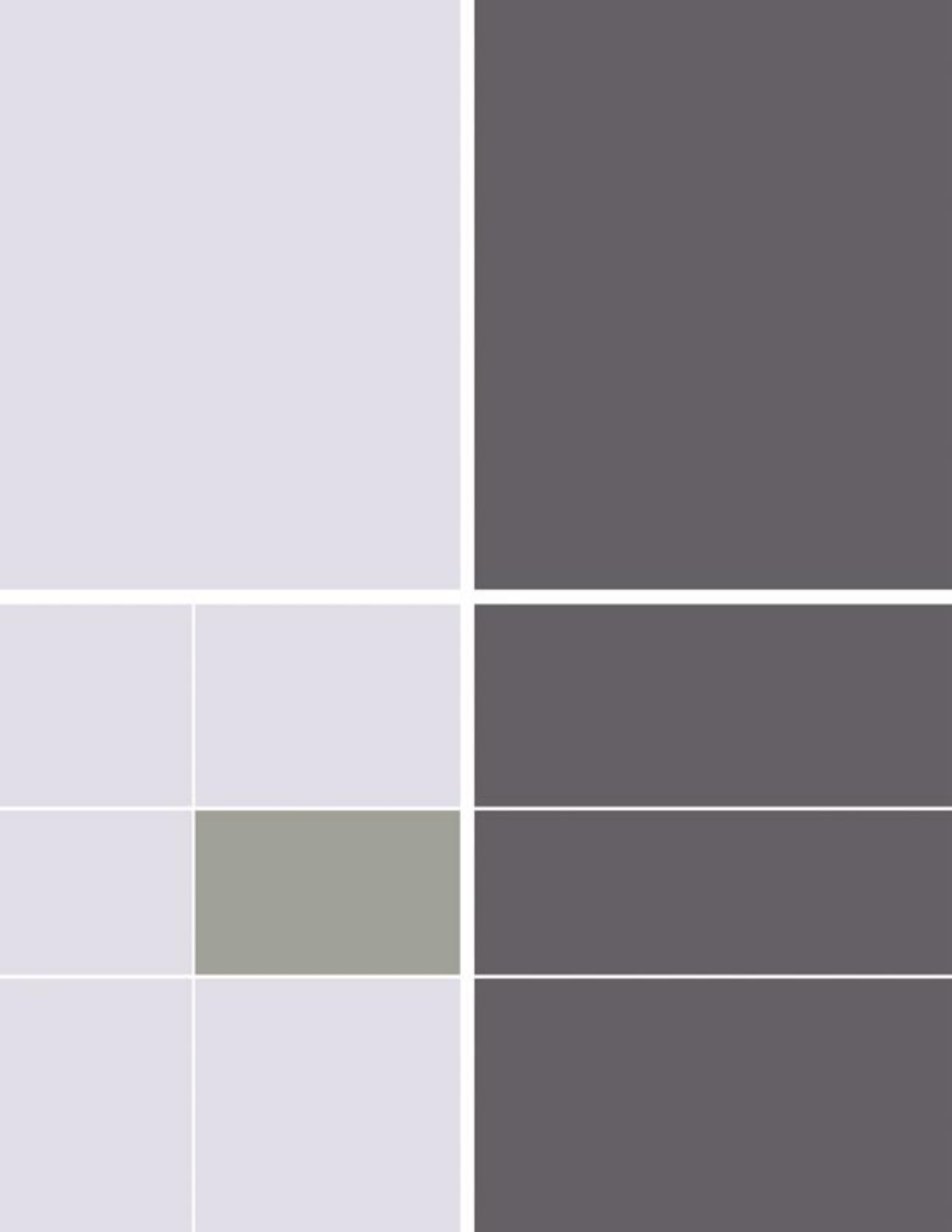


Plasma Physics Research Highlights





Understanding Mix in Inertial-Confinement Fusion

G.A. Kyrala, C.R. Christensen (P-24), M.A. Gunderson, D.A. Haynes, D.C. Wilson (X-2)

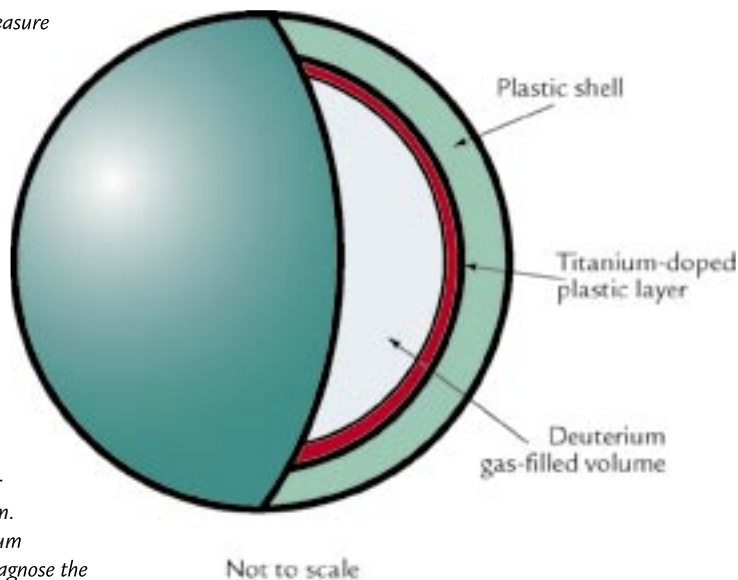
From the distant twinkle of the stars to the glowering fire of New Mexico at midday, fusion powers the universe. The Plasma Physics group (P-24) is at the forefront of the quest to capture this clean, safe, inexhaustible energy source here on earth.

In the inertial-confinement fusion (ICF) approach to fusion research, powerful lasers squeeze tiny capsules (Figure 1) filled with deuterium and tritium (rare forms of hydrogen) to enormous density and temperature to release huge amounts of nuclear energy and harmless helium gas: deuterium + tritium \rightarrow helium + neutron. This reaction could produce a megawatt of power (the same as a typical power plant) by burning only six millionths of an ounce of fuel per hour. The fuel is separated from seawater and is considered inexhaustible on conceivable time scales.

Mixed Impurities Reduce Nuclear Yield

One unsolved difficulty standing in the way of achieving fusion power is the problem of mix. During ICF implosions, internal temperatures can be around 140 million degrees Celsius, which is hotter than the core of the sun. The density can be 10,000 times what it would be at atmospheric pressure. Under these conditions, the material that forms the shell of the capsule (as well as the hydrogen fuel) is stripped of its electrons and becomes a highly reactive state of matter called a plasma. If this material mixes into the fuel, it interferes with fusion for several reasons. The heavier atoms of the shell are copious radiators, like a miniature version of the carbon arc

Figure 1. Researchers measure the spatial and temporal profiles of radiative emission from a thin titanium shell when it mixes during an ICF implosion. This measurement of the emission "color" and magnitude will constrain different mix models. The targets are shells of plastic with a titanium-doped layer on the inside surface of the shell. The target is filled with either 3 or 15 atm of deuterium. Emission from the titanium dopant will be used to diagnose the conditions in the core.



searchlights used to light up the sky at grand openings. When heated, the heavier elements release many electrons, increasing the particle density and contributing to the pressure of the hot, dense plasma resisting the force of the lasers. Thus, a capsule with a lot of mix cannot be squeezed down to the high fuel density and temperature that a clean capsule could. In addition, mix dilutes the fuel, so that within the 100 trillionths of a second or so that the burn takes place, fewer of the interparticle collisions are between the fuel nuclei, so

the burn gives less yield. For these reasons (i.e., radiating away the energy needed for heating, interfering with compression, and diluting fuel), mix diminishes the amount of energy we get from ICF implosions. To obtain a practical energy source to replace fossil fuels, the fusion reaction must produce enough energy beyond what is required to power the lasers used to implode the fuel capsules so that the scheme will be economically attractive. Mix diminishes energy output, so it's an important part of the economic equation.

RESEARCH HIGHLIGHT PHYSICS DIVISION

Plasma Physics Research Highlights

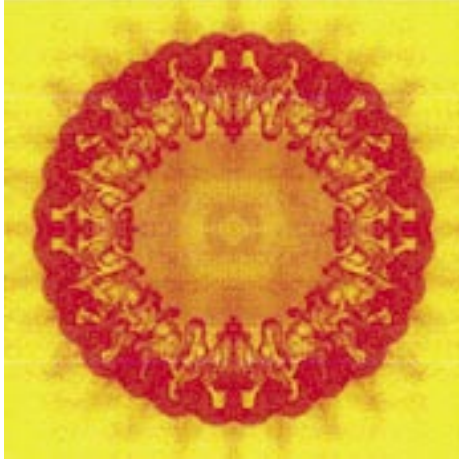


Figure 2. A supercomputer calculation of turbulent mix in an ICF capsule. The shell material is shown in red; the yellow in the center depicts the fuel. Turbulence develops during the implosion under the influence of hydrodynamic instabilities.

Mix occurs in ordinary states of matter (liquids or gases) because the molecules or atoms are in ceaseless random movement. The nuclei and electrons that comprise a plasma are in violently agitated motion with the particles traveling long distances without colliding. Thus, mix produced by random motion is greatly enhanced. Unfortunately, this component is only a miniscule part of the problem. Figure 2 depicts the results of a supercomputer simulation at a point in time midway during an ICF implosion (not necessarily our particular experiment). Turbulence develops as the capsule converges under the pressure from the lasers. Anyone who has dropped food coloring into water has seen these turbulent swirls and eddies. Similar behavior can be seen in the smoke from a smokestack or in a pot of boiling water. In ICF, the growth of turbulence is much more virulent, because the interface between a lighter material and a heavier material that accelerates it is inherently unstable. Many theories exist that attempt to model this turbulence behavior. They are difficult to verify in the ICF regime because present diagnostics cannot see the individual swirls looking through the edge of the spherical capsule, which is less than a millimeter in diameter.

Thus, while it is probably not possible to eliminate mix entirely, it is crucial to understand it. This understanding will enable us to mitigate the problem as much as we can and also to direct future research based on correct predictions.

P-24 Implosion Experiments Capture Images of Mix

Recent experiments performed by P-24 with collaborators from Applied Physics Division use a thin layer of titanium on the inside surface of a capsule (Figure 1) to image mix in the x-ray region. Titanium (22 electrons per atom) is used as the tracer element because it typically keeps at least one electron throughout the implosion, even at the core. Therefore, it still radiates efficiently at these high temperatures. The distribution of different “colors” of x-ray emission depends on the density and temperature in whatever local vicinity the titanium atoms find themselves.

Even if we cannot image the individual eddies, our results can still be used to reject models that do not match the energy distribution of the titanium emission versus radius and time.

Figure 3. Time history of the implosion. Time increases from right to left along a row, then from top to bottom. The circular images in the top two rows show the implosion of the 860 μm diam capsule during the time when the driving laser is on. Sixty laser beams with 22 million million watts (terawatts) of power produce an irradiance of a PW/cm^2 (a petawatt or a thousand million million watts per square centimeter) during a pulse lasting a billionth of a second. For comparison, the irradiance of the sun on the earth is $0.1 \text{ W}/\text{cm}^2$. The capsule is big enough in the beginning that the images for successive times overlap. The third row shows the inertial phase—the lasers are no longer on, but the capsule continues to implode. The fuel is ultimately compressed to 138 times its original density. Nuclear burn of the fuel begins 2200 ps after the start of the laser pulse. The last row shows an outgoing shock wave interacting with the still imploding outer part of the shell.

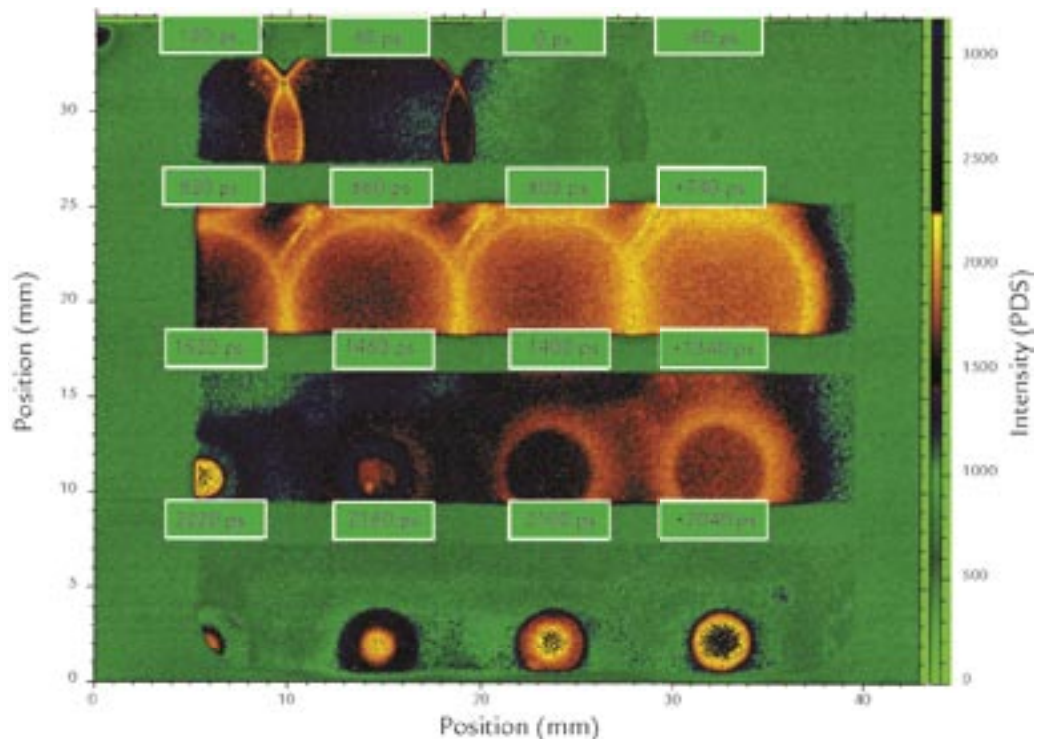
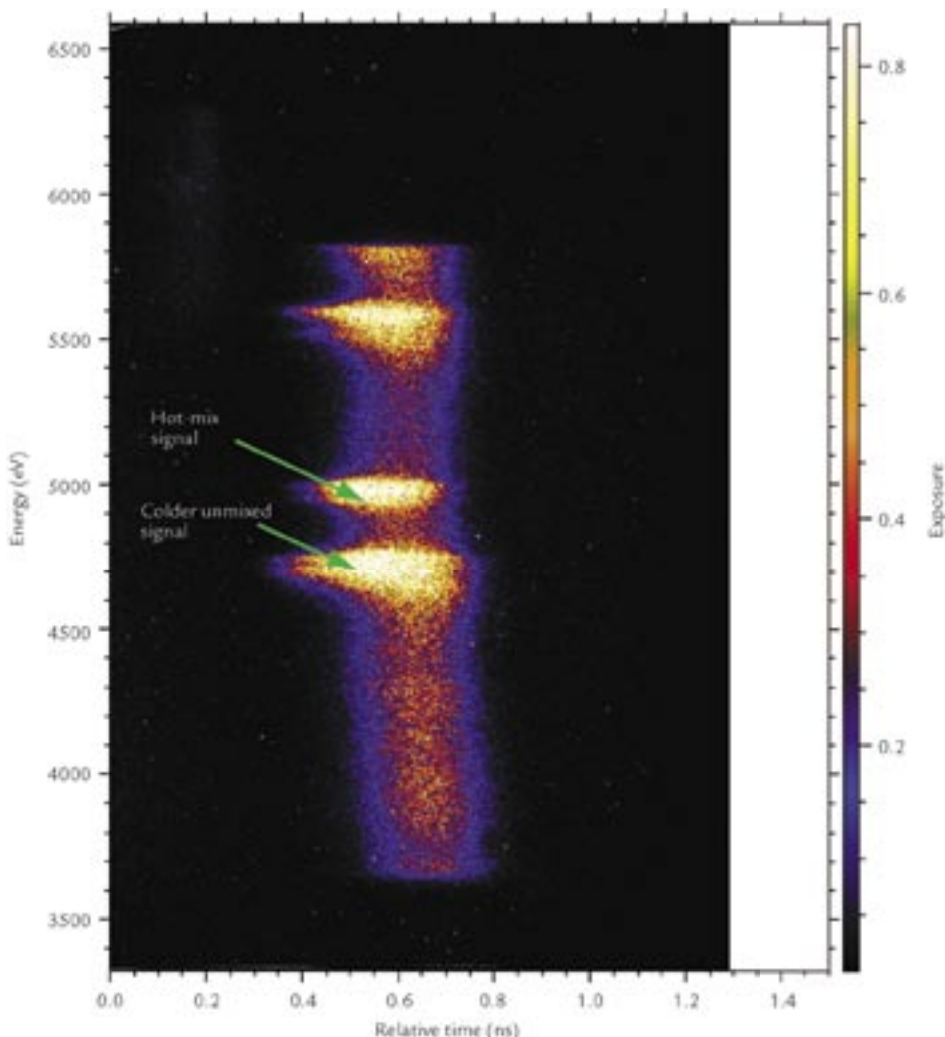


Figure 4. This time-dependent spectrum obtained in an experiment at the Omega laser facility shows the history of mixing of titanium from the shell during an implosion. Time is along the horizontal axis; x-ray radiation from the implosion is spread out along the vertical axis by a diffracting crystal, which disperses the x-rays according to their energy. Color on this plot is used to indicate the relative intensity (exposure) at each energy. The bright narrow band at ~ 5000 eV is the hydrogen-like titanium alpha line, and the helium-like line appears at ~ 4700 eV. The ratio of the signals in these lines changes as the titanium makes its way into the hot center.

Figure 3 shows x-ray framing camera images from our experiments. A framing camera produces a “movie” of the implosion, much like a movie camera produces a reel of film. However, in a framing camera, the film remains motionless, and the sensitive area that forms an image at any instant is determined electronically. The earliest picture is at the top right. As time progresses, the picture moves to the left and then down to the right edge of the next row. The time interval between two successive pictures is 60 ps, which corresponds to 17 thousand million frames per second. These images show the implosion, stagnation, and explosion of a capsule. The titanium shows up as brighter areas on the film. The interpretation is not simple because of the propagation of shocks. The increased noise on the film at stagnation is due to neutrons produced by the burn.

The time-resolved emission spectrum shown in Figure 4 is produced by a flat crystal located in front of a streak camera. From top to bottom, the radiation is separated by energy, or “color.” This is similar to the bands of colored light seen on a compact disc as it is tilted away from a light source. In our experiments, the different “colors” of light represent actual x-rays of different energies; therefore, a crystal is used to spread out the different energies. From left to right, the image



is swept in time. The camera puts the information onto an electron beam, which makes a picture from left to right in the same way that a television screen does. This image enables us to calculate the ratio of the titanium hydrogen-like alpha line (i.e., a transition from the second lowest atomic shell to the innermost shell when the electron making the transition is the last remaining one) to titanium helium-like alpha (i.e., the same transition when the atom still has one other electron that does not participate). The ratio of emission amplitudes in the two x-ray lines is important because the line from the hydrogen-like atoms is radiated only from the hottest part of the core. The ratio as a function of time allows us to watch the mixed material migrating into the center.

Conclusion

Our experimental series has just begun, so we are only beginning to interpret the implications for mix. We plan to carry these experiments further to measure not only where the mix occurs but also how much material is mixed into the fuel. We will use a series of capsules with the titanium layer buried successively deeper from the inside surface of the plastic. At the point in this series at which we no longer see a titanium signal, we will know that the thickness of the layer participating in mix is less than the burial depth. We continue to formulate refinements in the design of these exciting experiments.

Plasma Physics Research Highlights

Suggestions for Further Reading

1. D.K. Bradley *et al.*, “Measurements of core and pusher conditions in surrogate capsule implosions on the OMEGA laser system,” *Physics of Plasmas* **5**, 1870–1879 (1998).
2. D.D. Meyerhofer *et al.*, “Inferences of mix in direct-drive spherical implosions with high uniformity,” *Plasma Physics and Controlled Fusion* **43**, A277–A286 (2001).
3. V.A. Smalyuk *et al.*, “Hydrodynamic growth of shell modulations in the deceleration phase of spherical direct-drive implosions,” *Physics of Plasmas* **10**, 1861–1866 (2003).
4. S.P. Regan *et al.*, “Shell mix in the compressed core of spherical implosions,” *Physical Review Letters* **89**, 085003-1–085003-4 (2002).
5. M. Gunderson *et al.*, “Utilizing emission spectroscopy to study time-dependent mix,” European Conference on Laser Interaction with Matter, Los Alamos National Laboratory report LA-UR-04-6088.

Acknowledgment

This work was performed at LANL under the auspices of the U.S. DOE under contract No. W-7405-Eng-36. Experiments were performed on the Omega laser at the Laboratory for Laser Energetics (University of Rochester). General Atomics fabricated our capsules.

For further information, contact George Kyrala, 505-667-7649, gak@lanl.gov.



The World's Greatest Science Protecting America

Los Alamos National Laboratory, an affirmative action/equal opportunity employer, is operated by the University of California for the U.S. Department of Energy under contract W-7405-ENG-36.



Beryllium Ablator Microstructure and Stability Experiments

J.A. Cobble, T.E. Tierney, D.C. Swift (P-24), N.M. Hoffman, D.L. Tubbs (X-1),
A. Nobile, R.D. Day (MST-7)

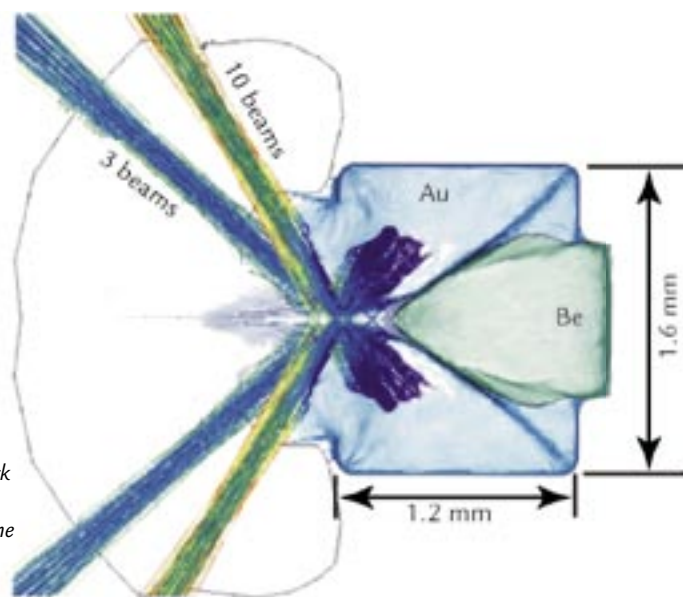
Controlled fusion in the laboratory remains the unfulfilled grand challenge of the nuclear age.

Fusion ignition of an inertially confined fuel capsule is a demanding task.¹ As in building a fire, the first task is assembling the fuel mass; however, for inertial-confinement fusion (ICF), this is extremely more difficult than collecting firewood.

The fusion fuel must be compressed to a density of $\sim 400 \text{ g/cm}^3$, which is over 30 times the density of solid lead and must be maintained at this density while its temperature is raised to over 200,000,000 K. Fuel assembly begins with as high a density fuel as possible—in this case, a thin shell of cryogenic deuterium-tritium (DT) ice at $\sim 18 \text{ K}$. The surface of the shell, both inside and outside, must be smooth to $\sim 1 \text{ }\mu\text{m}$,² and the radiation drive, which compresses the fuel, must be uniform to better than 1%.¹ These specifications are necessary to prevent hydrodynamic instabilities, which, while the irradiated capsule wall is compressing the fuel within, can rip the wall apart, release the fuel, and mix wall material with the fuel that remains in the core at the central hot spot. Only the highest quality compression will result in the density and the temperature of fuel necessary for ignition.

The first ablator material to be considered for the capsule wall was plastic. However, the technical hurdles to be overcome to field a plastic shell containing cryogenic DT ice are immense and the cost is prohibitive ($\sim \$150$ million). An alternate to plastic, beryllium has higher density, which leads to shorter laser drive for ignition; lower opacity, which leads to a higher implosion velocity; higher tensile

Figure 1. A gold vacuum hohlraum with laser beams entering from the left. The 800 μm diam beryllium package is centered on the back wall to the right. Gold and beryllium plasmas are filling the target.



strength, which allows a DT-filled capsule to be handled at room temperature; and higher thermal conductivity, which also relaxes cryogenic requirements.² However, crystalline beryllium, a naturally anisotropic material, supports different sound speeds depending on the direction of propagation. As long as a beryllium wall remains in the solid state during compression for fuel assembly, velocity shear at the beryllium-DT interface could lead to unfavorable hydrodynamic effects, primarily the classical Rayleigh-Taylor (RT) instability.³ Physics Division

and Applied Physics Division are collaborating in experiments to determine the magnitude of this potential problem. Meanwhile, Material Science and Technology Division is working to reduce the size of beryllium grains so that the number of grains in the wall with random orientation smoothes the effect of non-uniform velocity fields. Eventually during the radiation drive, the shock heating of the beryllium will cause melt. Then, the question becomes whether the material retains sufficient memory of RT behavior to spoil the compression.

RESEARCH HIGHLIGHT

PHYSICS DIVISION

Plasma Physics Research Highlights

For ignition at the National Ignition Facility (NIF), the early-time radiation pressure on the beryllium capsule will be 1–2 Mbar, exactly in the region for beryllium melt. Thus, experimental verification of beryllium behavior under various drive conditions is important to the success of future ignition experiments at NIF. We are therefore conducting beryllium ablator microstructure and stability experiments at the University of Rochester's Omega laser. Our main objective is to measure RT-instability growth rates in beryllium, first in machined sinusoidal perturbations and then from individual grains of various preselected sizes with “face-on” x-ray radiography. RT-instability growth is to be stimulated by laser-driven radiation in a gold vacuum hohlraum for as many growth times as needed to achieve detectability. We adopted the preliminary goals of

- (1) fabrication, utilization, and characterization of a relatively long (~ 6 ns) Omega pulse shape (to enhance RT-instability growth),
- (2) characterization of the hohlraum x-ray radiation drive to verify our ability to produce a first shock of ~ 1 Mbar pressure,
- (3) an assessment of the rate of influx of gold from the hohlraum wall during the drive, and
- (4) acquisition of face-on x-ray radiographs to assess requirements for effective diagnoses.

Experimental Rational and Results

Omega experiments typically last from 0.5–3 ns, which is insufficient time to detect microstructure-induced RT-instability growth in the beryllium. However, the longer the laser pulse, the less energy that can be extracted because of conversion efficiency problems in generating the 351 nm laser light at Omega. Our aim was to stagger two separate laser pulse shapes to integrate the longer drive within our targets.⁴

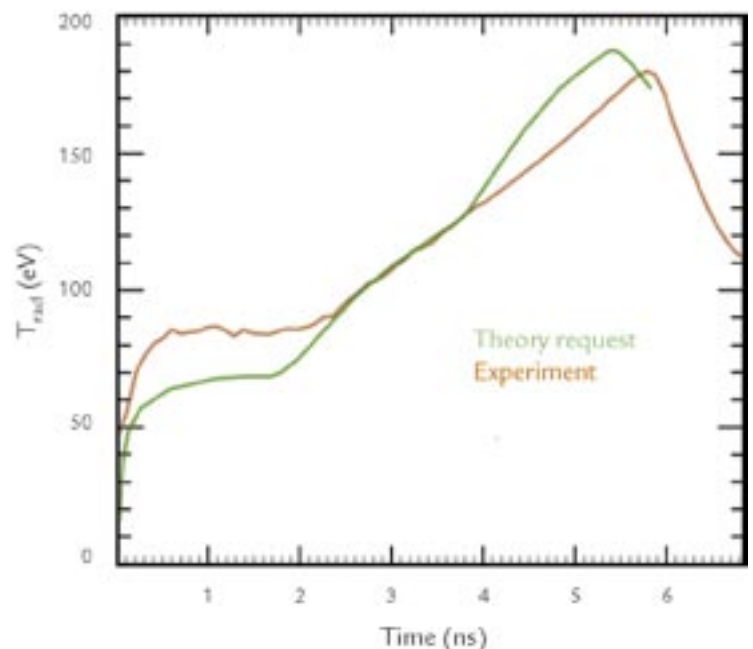
Then, after applying the appropriate laser drive to the hohlraum, we had to determine whether the measured radiation temperature, T_{rad} , and pressure, which drive the instability growth in the beryllium, matched theoretical predictions. Given the pulse length for heating the target, gold blowing in from the wall has sufficient time to stagnate on the hohlraum axis, blocking the later-arriving x-ray backlighter beam and hiding details of the RT-instability growth in beryllium, which has a much lower opacity than the gold. However, theoretical considerations suggest that radiation heating of the beryllium sample in the hohlraum could form a hot beryllium plasma bubble, putting pressure on the gold plasma and inhibiting its influx. Therefore, our final task was to qualify the ability of the vacuum hohlraum to maintain high visibility of the beryllium package within for face-on radiography.

Following initial laser profile design, we worked with Omega personnel to create two pulse shapes that when combined produced the desired ~ 6 ns laser drive. The integrated pulse consists of three beams carrying the “foot” of the drive for > 3 ns followed by ten 2.5 ns triangular-shaped beams, which carry

the bulk of the energy into the hohlraum. The timing of the foot drive and the triangular drive must be exact to within tens of picoseconds to maintain a smooth transition between the two sets of laser beams, which are symmetrically placed in azimuth around the wall of the hohlraum. Figure 1 indicates the placement of the laser pulses into the hohlraum target with a prediction, arising from a hydrodynamic model, for the position of the beryllium bubble with the application of over 4 kJ of laser energy.

T_{rad} was monitored by Dante, a ten-channel, filtered-x-ray-diode array.⁵ The results were consistent from shot to shot and are illustrated in Figure 2 with the desired radiation drive. Although it appears that T_{rad} is too high initially, the Dante measurement is increasingly less reliable below ~ 100 eV. For that reason, we also employed VISAR, a velocity interferometry system for any reflector⁶, to measure the free surface velocity of the beryllium sample, the shock-break-out time, and the radiation pressure. The ongoing VISAR analysis shows that during the first 3 ns, the radiation pressure is indeed about 1 Mbar.

Figure 2. Comparison of requested and measured T_{rad}



A gated x-ray framing camera (XRFC) filtered for gold M-band emission at 2.5 keV was used to monitor influx of gold from the hohlraum walls over the course of the radiation drive. Axial images in Figure 3 show the radial progress of the gold. During the third nanosecond of drive (at 10.5 mm on the y axis of Figure 3), the slowest component of the gold has moved $\sim 300 \mu\text{m}$ at a speed of $\sim 3 \times 10^7 \text{ cm/s}$. The fastest gold ions already appear to have stagnated on axis by 4 ns into the drive as shown by the black dot in the centers of the images. By 5 ns, the gold emission from the laser entrance hole (LEH), where the crossing laser beams have highest intensity, is heavy and uniform.

To assess the face-on radiography, we placed a gated axial XRFC opposite the LEH to the right of the beryllium sample in Figure 1 and, using M-band radiation from the LEH, backlit the beryllium, which for the first experiments was machined with a sine wave having a $100 \mu\text{m}$ period and an amplitude of $2.5 \mu\text{m}$. Figure 4 shows images from a single strip line from the XRFC taken at 5 ns into the laser pulse. The RT-instability growth of the sinusoidal variations has grown to the threshold of visibility as seen in modulations of the exposure, and an underexposed region near the hohlraum axis is revealed. Through analysis of parallax from the adjacent pinholes on the strip line, the center of mass of this quasi-opaque region is found to be one-quarter of the way back from the LEH—at exactly the position on axis where gold is not illuminated by laser beams. This observation provides evidence for an extensive beryllium bubble blowing out from the beryllium sinusoid, but which unfortunately does not reach far enough forward to prevent gold from obscuring the view.

Future directions

In the 20 laser shots for this campaign to date, we have learned that we can join different laser pulses together in a hohlraum to create a smoothly varying 6 ns radiation drive to study RT-instability growth in beryllium samples. Our first

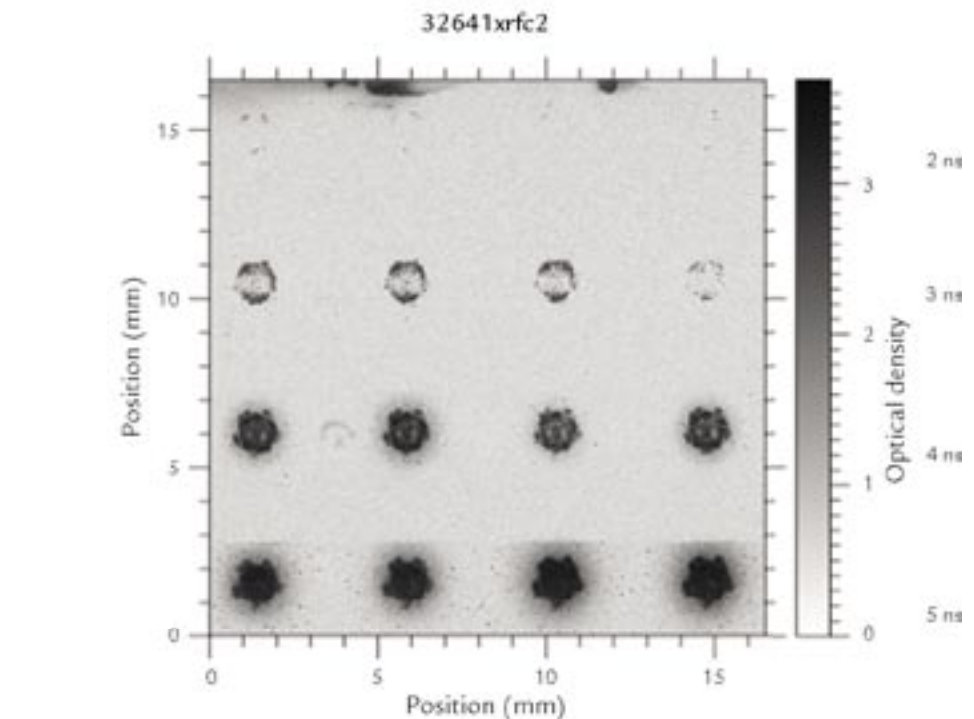


Figure 3. Gated XRFC images indicate the quasi-three-fold symmetry of the foot drive at 2 and 3 ns. (The time for each strip line of the imager is at the right in the figure. Time increases at $\sim 2 \text{ pt } 2 \pi \times 60 \text{ ps/frame}$, right to left.) The ten triangular-drive beams are paired, yielding quasi-five-fold symmetry later in time. These ten “turn on” at 3.5 ns.

effort has apparently resulted in a 1 Mbar drive, as measure by VISAR, which Dante confirms reaches $\sim 180 \text{ eV}$ at its peak, as required by theoretical demands. However, we have measured the influx of gold in a vacuum hohlraum and find that it is a threat to successful radiography. X-ray backlighting of sinusoidally perturbed beryllium samples has produced evidence

of RT-instability growth and of the presence of the beryllium bubble, which only partially inhibits gold plasma from encroaching into the center of the target. In the future, we hope to solve the gold influx problem with gas-filled targets, for instance, with 1 atm of CH_4 . Issues surrounding the gas-filled targets include the drive penalty for heating the gas—as

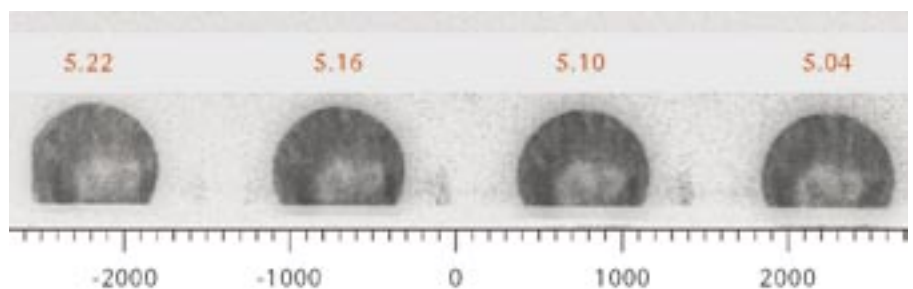


Figure 4. The 5 ns strip of the XRFC images for Omega shot No. 32652 shows the $100 \mu\text{m}$ sine wave in the beryllium sample and a region of quasi-opacity ($\sim 12\%$ transmission) shifting from frame to frame because of parallax. Gating times (ns) are in red; displacement (μm) is in object plane units.

Plasma Physics Research Highlights

much as a few hundred J—and possible laser-plasma instabilities. The latter may cause backscatter of 10% or more of the laser light away from the target. A drop in T_{rad} of ~ 10 eV is expected. The overall pulse duration might need to be shortened to boost the laser energy available for the required drive. Hopefully, laser energy will be available to evaluate a pulse shape for a 2 Mbar drive. We are encouraged that an Omega hohlraum environment can be created to validate beryllium as the material of choice for NIF ignition experiments.

Experiments at the Trident Laser Facility

Related laser-ablation experiments have been performed at the Trident Laser Facility at LANL to measure the strength of beryllium on a nanosecond time scale. The elastic and plastic response was monitored with VISAR from the sample surface and by *in situ* x-ray diffraction from the shocked beryllium. The effective strength was several times greater than that on the previously explored microsecond scales. These experiments also allow us to measure spatial variations in response caused by the microstructure of the material. Together with the Omega results, we are obtaining the detailed understanding of beryllium properties needed to set requirements for indirect-drive ignition experiments on NIF.

References

1. J. Lindl, “Development of the indirect-drive approach to inertial confinement fusion and the target physics basis for ignition and gain,” *Physics of Plasmas* **2**, 3933–4024 (1995).
2. D.C. Wilson *et al.*, “The development and advantages of beryllium capsules for the National Ignition Facility,” *Physics of Plasmas* **5**, 1953–1959 (1998).
3. N.M. Hoffman *et al.*, “Microstructure, shock waves, and stability: The initiator of mixing?” *Bulletin of the American Physical Society* **48**(7), 255 (2003).
4. D.L. Tubbs and N.M. Hoffman, “3- ω laser pulse shapes for July 2003 beryllium ablator microstructure and stability (BAMS) experiments at Omega,” LANL memo X-1: 2003-005, March 28, 2003.
5. H.N. Kornblum *et al.*, “Measurement of 0.1–3 keV x-rays from laser plasmas,” *Review of Scientific Instruments* **57**, 2179–2181 (1986).
6. D.L. Paisley *et al.*, “High-speed optical and x-ray methods for evaluating laser-generated shock waves in materials and the corresponding dynamic material response,” *Proceedings of the International Society of Optical Engineering (SPIE)* **4183**, 556–565 (2001).

Acknowledgment

This work has been done under the auspices of the U.S. DOE. We acknowledge the expert assistance of many workers at the University of Rochester Laboratory for Laser Energetics, including resident staff from Lawrence Livermore National Laboratory.

For further information, contact James Cobble, 505-667-8290, cobble@lanl.gov.



The World's Greatest Science Protecting America

Los Alamos National Laboratory, an affirmative action/equal opportunity employer, is operated by the University of California for the U.S. Department of Energy under contract W-7405-ENG-36.



Ultra-High-Intensity Laser Physics at the LANL Trident Laser Facility

B.M. Hegelich, J.C. Fernández, J.A. Cobble, K.A. Flippo (P-24), B.J. Albright, E.S. Dodd, M.J. Schmitt (X-1), R. Perea (MST-7)

Modern ultra-high-intensity lasers are able to reach focal intensities of the order of 10^{18} – 10^{21} W/cm² where laser-plasma interactions become relativistic, and a variety of new effects emerge into a completely new regime of physics. These processes include relativistic self-focusing of the laser beam, which results in even higher intensities, laser-induced particle acceleration to MeV energies on a μ m scale, x-ray lasers, laser-induced nuclear physics, and even the production of antimatter and other exotic particles. These effects can be applied to a variety of physics studies and can potentially be used for a number of applications. Concepts under consideration are next-generation accelerators, the jump-starting of inertial-confinement fusion with fast ignition, various medical applications, and laboratory astrophysics. One of the three beams of the Trident laser facility at LANL has been converted to deliver ultrashort laser pulses at the above-mentioned intensities so that researchers can participate in this exciting new field at the forefront of today's physics. This beam is used to carry out a program that investigates the acceleration of ion bunches to MeV energies and MA currents and the interaction of these ions with different targets.

High-Irradiance Laser-Matter Interactions

An ultra-high-intensity laser pulse pointed at a solid target always interacts with a plasma because of its finite contrast ratio. Even in a laser with a relatively excellent contrast of $\sim 10^{-7}$ there will be a “pre-

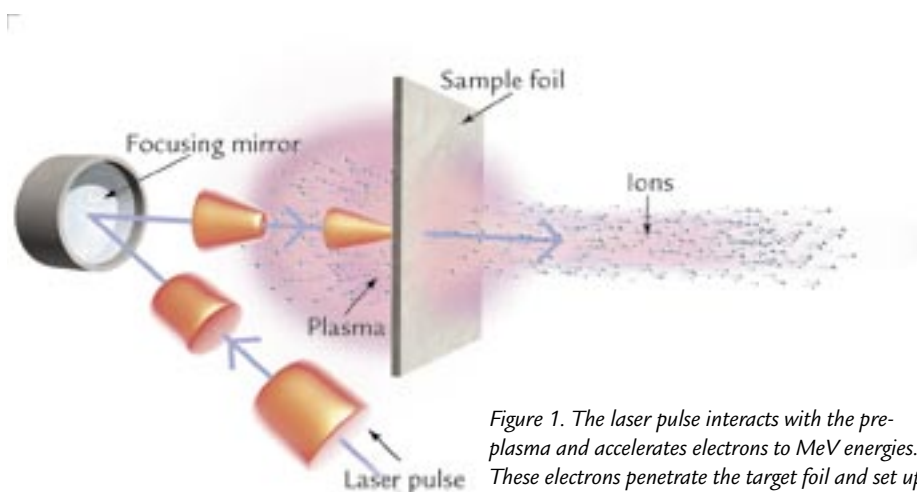


Figure 1. The laser pulse interacts with the pre-plasma and accelerates electrons to MeV energies. These electrons penetrate the target foil and set up an MV/ μ m quasi-static electric field that ionizes and accelerates the rear surface atoms.

pulse” at 1–2 ns ahead of the main pulse with an intensity above 10^{12} W/cm², which is high enough to instantly create a plasma. The main pulse will therefore always interact with a plasma and never with a solid target. Furthermore, at these intensities, the laser-plasma interaction is relativistic, i.e., the electrons gain energy on the order of their rest mass when moving in the electro-magnetic field of the laser pulse. The laser transfers energy to the electrons and accelerates them in the laser-propagation direction through the target to multi-MeV energies. This process is due to the $\mathbf{v} \times \mathbf{B}$ force from the magnetic component of the electromagnetic

field, which becomes nonnegligible when v approaches the speed of light. As illustrated in Figure 1, the electrons will penetrate a thin foil target, exit out the back surface, and set up a virtual cathode—a very strong electric field, exceeding field strengths of a few 10^{12} V/m (TV/m).

The electric field ionizes the rear surface and accelerates whatever ions are situated there to energies of many MeV. Protons have been accelerated to more than 60 MeV,¹ fluorine ions to above 100 MeV,² and lately high-Z palladium ions to 220 MeV.^{3,4} In many beam parameters, those ion pulses now exceed those of

RESEARCH HIGHLIGHT PHYSICS DIVISION

conventionally accelerated ions by orders of magnitude, exhibiting pulse durations in the subpicosecond range, beam currents up to MA, and a transverse emittance $\epsilon_t < 0.001 \pi \text{ mm mrad}$.⁵ A typical conventional accelerator like the CERN Super Proton Synchrotron (SPS) has an emittance of $\epsilon_t < 1 \pi \text{ mm mrad}$. These parameters have rekindled interest in laser-accelerated ion beams for applications like proton radiography⁶, isochoric heating⁷, fast ignition⁸, and next-generation accelerators. The major difficulty for all these applications to date has been the large energy spread of the laser-accelerated ions, which typically exhibit a Maxwellian-like energy spectrum as shown in Figure 2. At LANL, we have demonstrated for the first time that quasi-monoenergetic ion beams can be generated by controlled target treatment before irradiating the metal foil target with an ultra-high-intensity laser. Furthermore, we also show the acceleration of a single charge state

of one ion species directly in the forward target-normal direction. The accelerated C^{5+} ion bunch shown in Figure 3 exhibits a longitudinal emittance of $\epsilon_l < 2 \times 10^{-6} \pi \text{ eV s}$, exceeding that of conventional high-current accelerators by orders of magnitude. This new result shows the strong potential impact that ultra-high-intensity laser physics can have in many other areas of physics.

Accelerated Ions

Due to the vacuum conditions in ultra-high-intensity laser experiments, which typically are around 10^{-6} mbar , all target surfaces are coated with water vapor and hydrocarbon layers, e.g., pump oil. That means that no matter what target material is used, the outer layer always contains protons. Because of its low ionization potential and because protons exceed every other ion's charge-to-mass ratio by at least a factor of two, they are more efficiently produced and accelerated, drain the energy out of the acceleration process, and screen the accelerating electric field for the heavier particles. Accelerating other ions therefore requires the removal of the contaminating proton layers. This removal was demonstrated by Hegelich *et al.*² using the 100 TW laser at the École Polytechnique LULI research center with carbon and fluorine ions. To achieve our goal of mid- to high-Z ion acceleration at LANL's Trident laser facility, we implemented the same kind of cleaning techniques in our ultra-high-intensity laser experiments. Trident delivers pulses of up to 30 J in as short as 600 fs, which corresponds to a power of $\sim 30 \text{ TW}$. As such, Trident is currently the highest-energy subpicosecond laser in the U.S. The beam is aimed at an off-axis parabolic mirror within a vacuum chamber to focus the beam from its initial diameter of 6 in. down to a $20 \mu\text{m}$ spot on the target, achieving intensities in excess of 10^{19} W/cm^2 . A sketch of a typical setup is shown in Figure 4.

To clean the target, we rely on two methods: Joule heating using either a strong direct current that is passed through

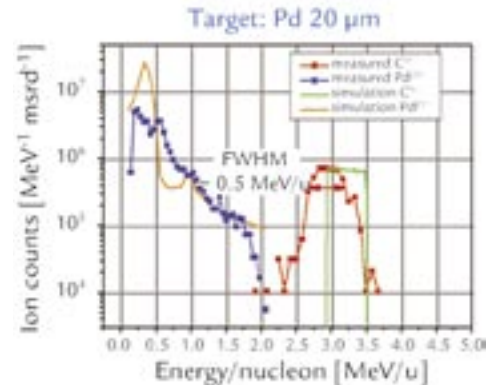


Figure 3. Measured ion energy spectra and simulations using BILBO.

the foil or a continuous-wave (cw) laser. Both methods are capable of heating the target to temperatures in excess of 1000°C , which remove all hydrogen-bearing contaminants. With no hydrogen present, remaining species on the rear surface are ionized by the electric field. The charge state with the highest charge-to-mass ratio is predominantly accelerated. Experiments on the LULI 100 TW laser and on the Trident laser successfully accelerated a wide range of low-Z ions to multi-MeV/nucleon energies. Figure 2(a) shows the spectra for helium-like beryllium, carbon, oxygen, and fluorine.

Moving from low-Z ions to mid- or high-Z ions proves to be more difficult. Although contaminants like water vapor can be cooked off by heating the target, heating cannot clean metal oxides, carbides, and nitrides on the surface—these contaminants usually have binding energies in the eV range. To overcome this problem we are working on two different approaches. The first approach is to use a second pulsed laser at relatively low intensity ($\sim 5 \times 10^{10} \text{ W/cm}^2$) to ablate the rear surface thus removing the contaminating oxides, etc. Although this approach worked in principle, the technical details are tricky and remain a subject of ongoing study. The second approach is to use a “magic” material that does not form oxides or other compounds. This approach is the easier solution, however, it limits the available target

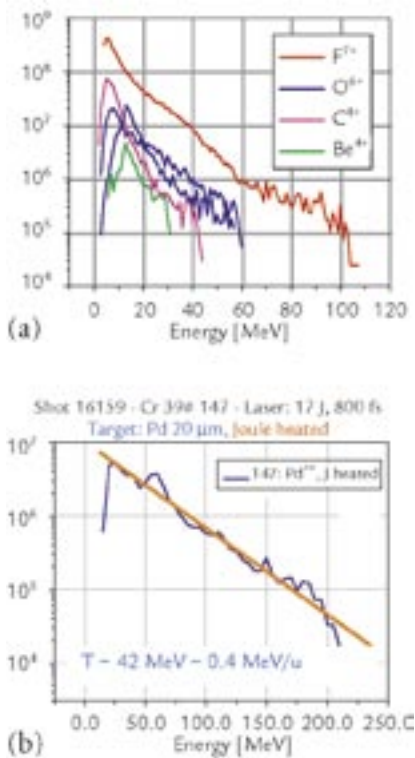


Figure 2. (a) Typical low-Z ion spectra from both the LULI 100 TW laser and Trident. (b) First mid-Z ion spectra [palladium(22^+), $Z = 46$] from Trident.

materials. One such “magic” material is palladium. With an atomic mass of 106, palladium ($Z = 46$) does not easily form oxides. As shown in Figure 2(b), we succeeded for the first time to accelerate a mid- Z material into a multi-MeV/ nucleon-ion bunch using an ultra-high-intensity laser. In future experiments, we hope to improve this result, increasing the energy and the particle number and achieving greater control of the beam properties, e.g., ballistic focusing as shown in Figure 3. Once these goals are achieved, the palladium beam can be used to study isochoric heating in matter, effectively recreating in the laboratory conditions that are otherwise only found in the interior of large Jovian-like planets.

Monoenergetic Ions and Modeling

As mentioned earlier, we were the first to accelerate a monoenergetic MeV-ion bunch with a laser. When heating the palladium target to remove the hydrogen, a thin monolayer layer of carbon atoms remained at the rear surface. Because these carbon layers are very localized, all carbon atoms see the same field at the peak of the

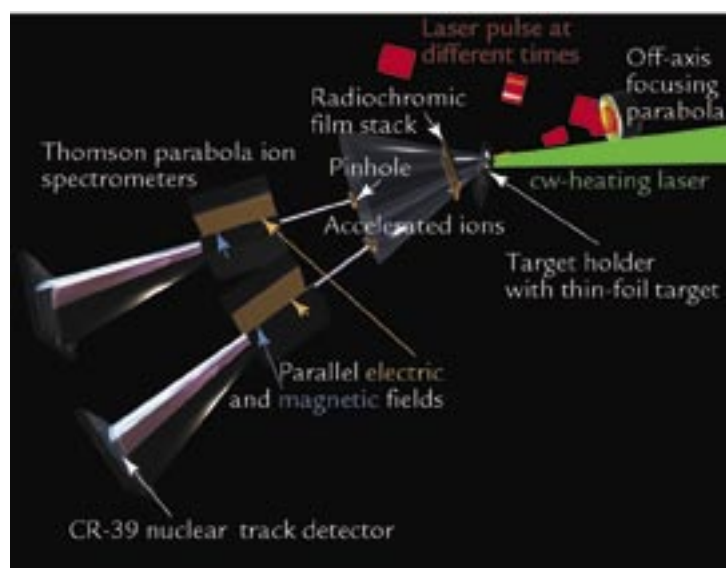


Figure 4. Typical setup of a laser-ion-acceleration experiment. The target is typically a $\sim 10 \mu\text{m}$ thin metal foil, the diagnostics consist of various films, track detectors, and spectrometers. A green cw laser is used to clean the target of hydrocarbon contaminants.

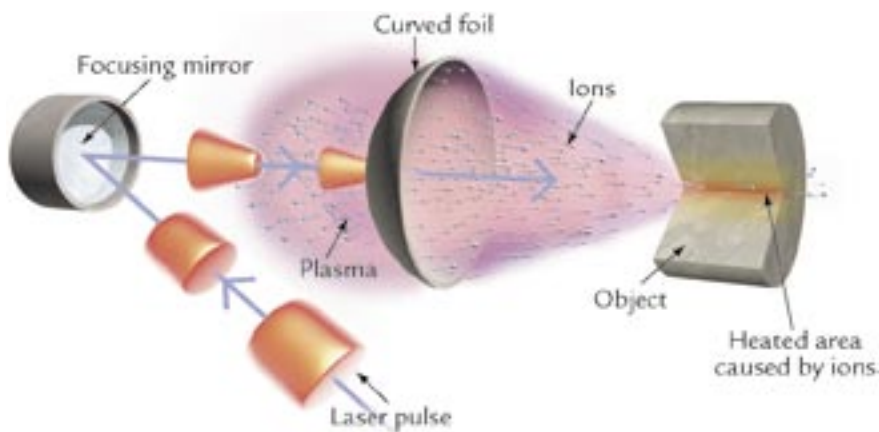


Figure 5. Ballistic focusing of a laser accelerated ion beam into a secondary target. The secondary target will be heated isochorically to high temperatures while remaining at high density, recreating conditions found in the core of Jovian-like planets.

pulse and are ionized to the same charge state and instantly accelerated. As the field decreases after ~ 100 fs, all the carbon atoms are at the front of the ion expansion, in a position trailing the hot electrons, which effectively conserves their volume in phase space. The full width half maximum of 0.5 MeV per nucleon in the Thomson parabola spectrum shows a longitudinal emittance of this C^{5+} bunch smaller than 2×10^{-6} eV seconds—about six orders of magnitude better than for the CERN SPS.

We have used the one-dimensional hybrid code BILBO (Backside Ion Lagrangian Blow-Off) to help us understand this result. BILBO solves a Vlasov-Maxwell system analytically, calculating the boundary conditions for a nonlinear Poisson solver. The solver yields the electron density

and electric fields and propagates the ions as kinetic particles. The code uses a threshold ionization model with atomic data for ionization energies of carbon and palladium and hot-electron-cooling models to account for the extraction of energy used to accelerate the ions. Using BILBO, we reproduced the measured spectra qualitatively (Figure 3) and seek to derive better models to understand and optimize beam production.

Conclusion

Future experiments will be directed towards better understanding of the underlying acceleration physics and towards the use of the accelerated ions for a number of different applications. Because of the modest integrated energy of the ions, they must be focused to one point, which can be achieved by using curved targets (Figure 5). The long-term goal of our project is to study transport and stopping mechanisms of high-current ion beams in cold, dense plasmas. These experiments require the use of Trident’s other beam lines to create the target plasma while the short-pulse beam generates the ion pulse. For these experiments and for other short-pulse physics applications, more energy in the short-pulse beam is desirable and in some cases even necessary. Therefore, the Trident

Plasma Physics Research Highlights

short-pulse arm will be upgraded over the next 18 months to deliver pulses of ~ 115 J in less than 500 fs. This 200 TW upgrade puts Physics Division even more firmly at the forefront of modern science and opens new opportunities for programmatic research. It keeps Trident among the best of the existing short-pulse lasers in the world and makes even more exotic new physics accessible.

References

1. R.A. Snavely *et al.*, "Intense high-energy proton beams from petawatt-laser irradiation of solids," *Physical Review Letters* **85**, 2945–2948 (2000).
2. B.M. Hegelich *et al.*, "MeV ion jets from short-pulse-laser interaction with thin foils," *Physical Review Letters* **89**, 085002-1–085002-4 (2002); [For nanosecond-laser work, resistive Joule heating was successfully accomplished by W. Ehler *et al.*, "Effect of target purity on laser-produced plasma expansion," *Journal of Physics D: Applied Physics* **13**, L29–L32 (1980).]
3. B.M. Hegelich *et al.*, "Spectral properties of laser accelerated mid-Z MeV/u ion beams," in *Proceedings of the 28th European Conference on Laser Interaction with Matter*, Rome, September 6–10, 2004.
4. J.C. Fernández *et al.*, "Laser-ablation treatment of short-pulse laser targets: Towards an experimental program on energetic-ion interactions with dense plasmas," in *Proceedings of the 28th European Conference on Laser Interaction with Matter*, Rome, September 6–10, 2004.
5. T.E. Cowan *et al.*, "Ultralow emittance, multi-MeV proton beams from a laser virtual-cathode plasma accelerator," *Physical Review Letters* **92**, 204801-1–204801-4 (2004).
6. J.A. Cobble *et al.*, "High resolution laser-driven proton radiography," *Journal of Applied Physics* **92**, 1775–1779 (2002).
7. P.K. Patel *et al.*, "Isochoric heating of solid-density matter with an ultrafast proton beam," *Physical Review Letters* **91**, 123004-1–123004-1 (2003).
8. M. Roth *et al.*, "Fast ignition by intense laser-accelerated proton beams," *Physical Review Letters* **86**, 436–439 (2001).

Acknowledgment

This work has been performed under the auspices of the U.S. DOE. We acknowledge support from 2004 Laboratory-Directed Research and Development/ Directed Research Proposal 20040064 and experimental run time at Ecole Polytechnique, Paris, France.

For further information, contact Manuel Hegelich, 505-667-6989, hegelich@lanl.gov.



The World's Greatest Science Protecting America

Los Alamos National Laboratory, an affirmative action/equal opportunity employer, is operated by the University of California for the U.S. Department of Energy under contract W-7405-ENG-36.



Inertial-Electrostatic-Confinement Fusion Device

*J. Park, S.M. Stange (P-24), R.A. Nebel (T-15),
K.M. Subramanian (University of Wisconsin)*

Inertial-electrostatic-confinement (IEC) systems provide an economical and technologically straightforward means to produce fusion reactions in a table-top device.^{1,2} IEC devices confine a plasma in a potential well created by electrostatic fields or a combination of electrostatic and magnetic fields. The fields can be produced either by grids or by virtual cathodes, typically in spherical or cylindrical geometry. The fields accelerate ions towards the center of the device, where fusion reactions can occur (Figure 1). The technological simplicity of the IEC system was the basis for its early success—it produced a steady-state neutron yield of 2×10^{10} neutrons/s in the late 1960s.³

Applications

One of the most promising applications for an IEC-based neutron source is the active nuclear assay of highly enriched uranium and high explosives (HE), such as landmines. High-energy neutrons (e.g., 14.1 MeV neutrons from deuterium-tritium [DT] fusion reactions) have the ability to penetrate shielded materials very effectively. For example, Monte Carlo neutron and photon (MCNP) transport-code calculations indicate that 14.1 MeV neutrons can penetrate soil as deep as 1 m and detect HE, such as landmines. We are currently working with a private company to develop a compact and economical intense neutron source based on the IEC system. The enhanced-detection capability of the IEC-based neutron source, compared to natural radiation sources, could provide cutting-edge technology for homeland defense and humanitarian causes.

Periodically Oscillating Plasma Sphere

Though useful for practical neutron sources, the existing IEC fusion devices suffer low fusion yields, $\sim 0.01\%$ of input power. This is because the Coulomb-collision cross section is much greater than the fusion-collision cross section by several orders of magnitude. The ion beams in the IEC device rapidly lose the energy by Coulomb collisions before producing fusion reactions, leading to a net loss in energy.

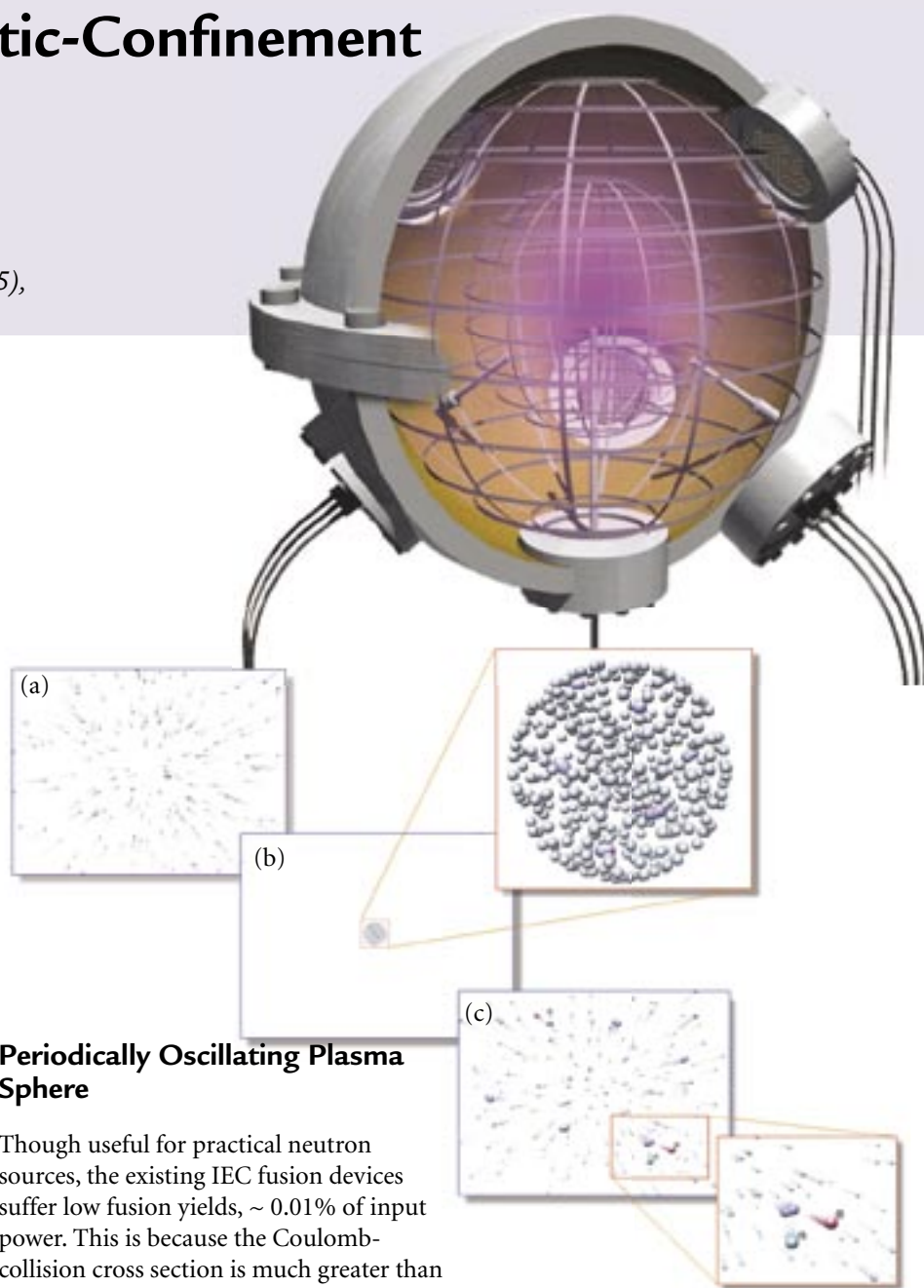


Figure 1. Grid-based IEC device. Fusion reaction occurs in the center region where the high-energy ions converge. The dynamics of a periodically oscillating plasma sphere (POPS) oscillation are shown as an (a) implosion, (b) compression, and (c) expansion.

RESEARCH HIGHLIGHT
PHYSICS DIVISION



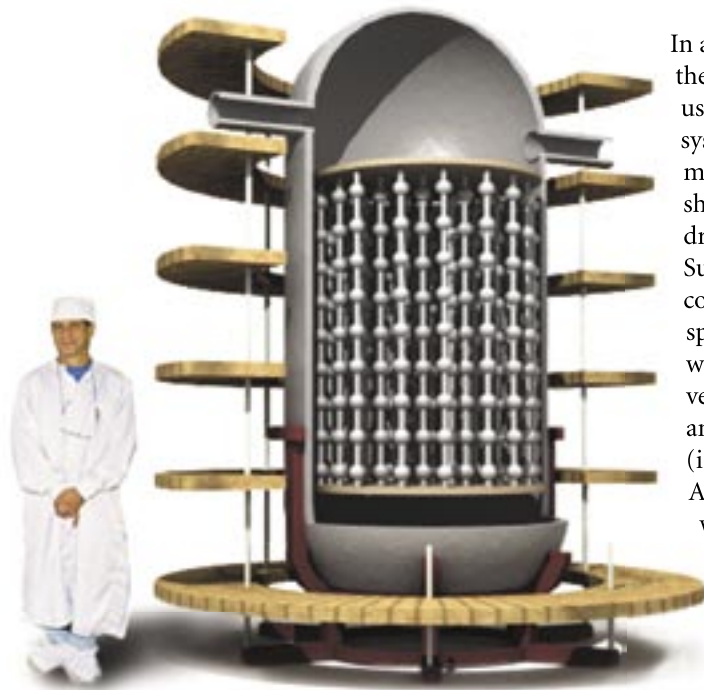


Figure 2. Penning trap modular IEC device for a high mass power density fusion reactor.

A new electrostatic plasma equilibrium that should mitigate this problem has been proposed by LANL theorists⁴ and recently confirmed experimentally.⁵ This concept requires uniform electron injection into the central region of a spherical device to produce harmonic oscillator potential. An ion cloud (referred to as the Periodically Oscillating Plasma Sphere, or POPS) in such an environment will undergo harmonic oscillation with an oscillation frequency independent of amplitude. Tuning the external radio-frequency (rf) electric fields to this naturally occurring mode allows the ion motions to be phase-locked. This simultaneously produces very high densities and temperatures during the collapse phase of the oscillation when all the ions converge into the center. Solutions to POPS oscillation have the remarkable property that they maintain equilibrium distribution of the ions at all times. This would eliminate any power loss due to Coulomb collisions and would greatly increase the neutron yield up to more than 100%, resulting in a net energy gain for fusion-power generation.

In a practical embodiment, the POPS system would use a massively modular system to achieve high-mass-power density as shown in the conceptual drawing in Figure 2. Such a device would contain thousands of tiny spherical IEC reactors within a single reactor vessel to produce a large amount of fusion power (i.e., $\sim 100\text{--}1000\text{ MW}$). A modular IEC device would have very high-mass-power density, comparable to a light-water reactor, while maintaining conventional wall loads ($\sim 1\text{ MW/m}^2$) and being economically competitive with other sources of power.

First Experimental Confirmation POPS Oscillation

The POPS oscillation has been experimentally measured for the first time, confirming the scientific basis for a POPS-based fusion device. The harmonic

potential well is created by electron injection.⁶ Ions in the potential well undergo harmonic oscillation. By applying rf fluctuation to the grid voltage, we were able to phase-lock the POPS oscillation and to measure the resonance behavior of the ions. Mathematically, ion dynamics during the driven POPS oscillation are equivalent to the driven harmonic oscillator as described by the Mathieu equations. The ions can gain a large amount of energy from a small external perturbation when the driving frequency is equal to the resonance frequency. The ion orbits become unstable, and ion loss from the potential well is enhanced. In the experimental setting, the enhanced ion loss compensates the background ionization and extends the lifetime of the potential well. On the other hand, rf fluctuation outside the POPS resonance frequency makes little impact to the ion loss. This resonance behavior of ion dynamics is shown in Figure 3, where the temporal variation of the plasma response is measured for various rf frequencies. Without rf fluctuation, the lifetime of the potential well is very short, $\sim 0.5\text{ ms}$, due to significant background ionization. By applying small rf fluctuation ($\sim 4\text{ V}$ amplitude compared to a direct-current [dc] bias voltage of 250 V) at POPS frequency, the lifetime increases greatly

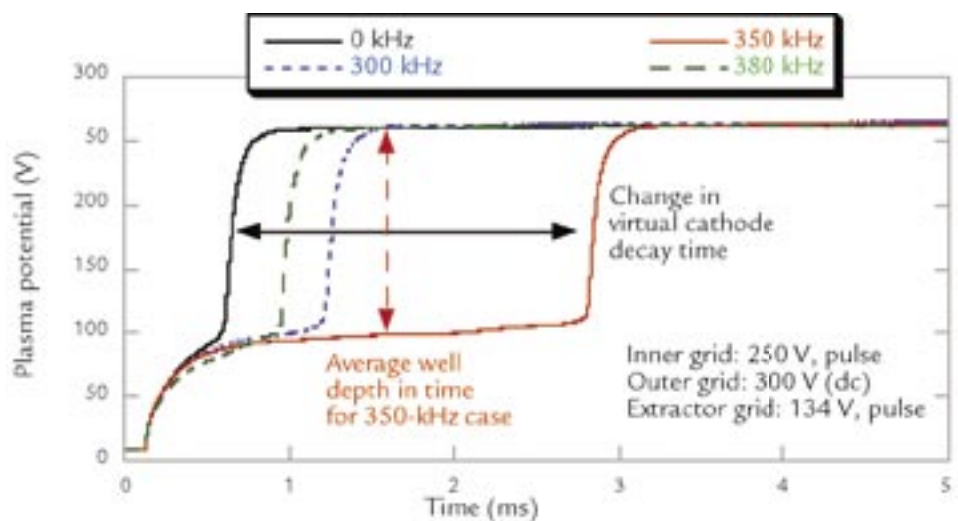


Figure 3. Temporal evolution of plasma potential at the center. The potential well lifetime is extended by applying rf fluctuation to the inner grid bias voltage at POPS frequency.

to ~ 2.5 ms. In comparison, rf fluctuation outside the resonance frequency changes the lifetime only slightly.

The frequency at which the POPS oscillation is found scales as $f_{POPS} = (\sqrt{2/\pi}) * (V_{well}/r_{well}^2 M_{ion})^{0.5}$. In using a harmonic-oscillator analogy, the ion mass provides the inertia, whereas the curvature of potential well is equal to the coefficient of the restoring force. Because this was the first time that the POPS oscillation has ever been experimentally observed, extensive efforts were made to verify the POPS frequency scaling as a function of the well depth and the ion mass. As shown in Figure 4, excellent agreement was obtained between the experiments and the theory, confirming that the observed resonance is the ion mode associated with the POPS oscillation. The potential well depth was controlled by varying the dc component of the inner-grid bias, whereas the well radius is fixed by the inner-grid dimension. Note that the well radius was estimated as $r_{well} = r_{grid} + \lambda_{Deff}$ where λ_{Deff} is the effective Debye length to account for the Debye shielding. We also varied the fill gas, using three different ion species, H_2^+ , He^+ , and Ne^+ to investigate the POPS frequency scaling.

Particle Simulation of POPS Plasma Compression

One of the most significant issues facing a fusion device based on POPS is the plasma compression, which determines the achievable fusion rates. In the case of deuterium-deuterium (DD) fuel, a radial plasma compression of 25 is sufficient for active nuclear assay, whereas the neutron tomography would require a compression of 100. In comparison, a practical fusion-power plant would require a compression of 2000 for DD fuel but less than 100 for DT fuel. One factor that greatly affects the compression ratio is the extent of space-charge neutralization. Inadequate space-charge neutralization can cause self-repulsion of the ion cloud during the collapse phase, limiting the compression.

A gridless particle code of one dimension in space and two dimensions in velocity space has been developed to investigate the space-charge neutralization during POPS compression.⁷ Figure 5 shows the radial profiles of ion density and plasma potential during POPS compression. The results in the left are from the expansion phase of POPS oscillation. The ion density profile is Gaussian in space, and the plasma potential profile matches the required harmonic oscillator potential for ions, produced by constant electron injection. In the middle, the ion density and the plasma potential during the collapsed phase of POPS oscillation are shown. A large distortion of plasma potential is due to the insufficient space-charge neutralization and ion self-repulsion during the POPS compression. This has limited the radial plasma compression to only 6.3. In comparison, the results on the right come from the case where we modulate the initial velocity distribution of injected electrons as a function of time to improve

the space-charge neutralization. This simple remedy helped to improve the space-charge neutralization in the core during the collapse phase. A radial plasma compression of 19 has been obtained, resulting in the ion-density enhancement of $\sim 10,000$ in the core as compared to the expansion phase. Currently, we are investigating a method, proposed by Louis Chacon (Plasma Theory Group, T-15), to correctly modify the injected electron distribution to eliminate the space-charge neutralization problem and to improve the plasma compression.

Conclusion

The IEC Team in our Plasma Physics Group (P-24) and T-15 is working on developing practical fusion devices based on an IEC scheme. The recent experimental confirmation of the POPS oscillation and successful plasma compression in a particle simulation has provided solid scientific foundation for

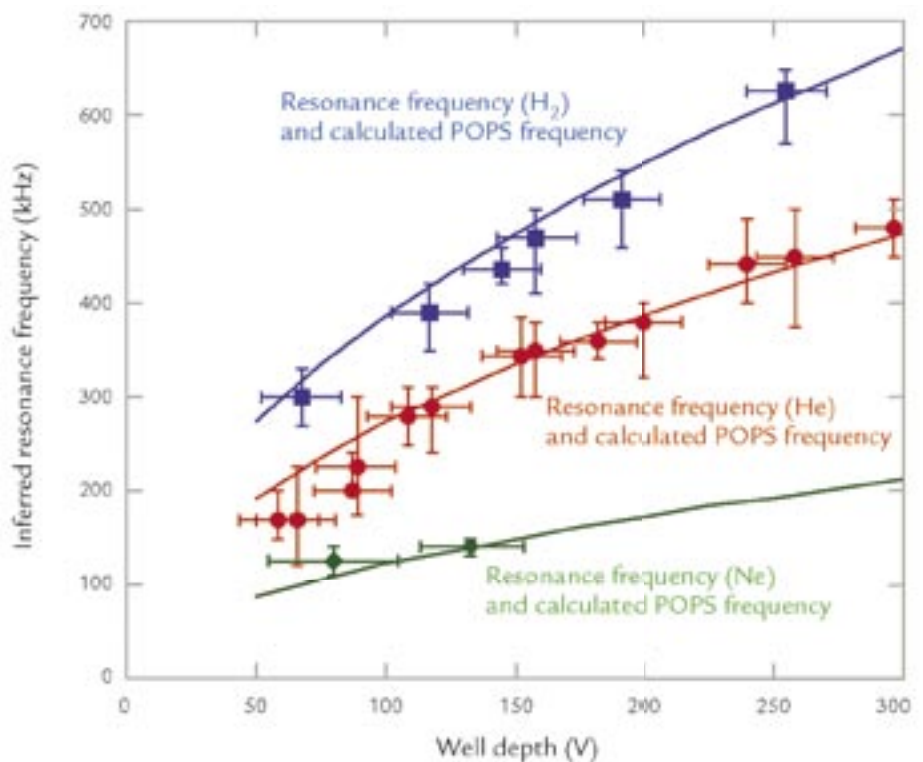


Figure 4. Comparison between the experimentally measured resonance frequencies due to POPS oscillation (points) and the theoretical calculations (lines) as a function of potential well depth and ion mass.

Plasma Physics Research Highlights

further exploration of this promising fusion device concept. This exploration will include direct experimental measurement of plasma compression and fully two-dimensional particle simulations of POPS dynamics. Successful plasma compression of at least 50 will be followed by a demonstration of nuclear fusion reactions using POPS.

References

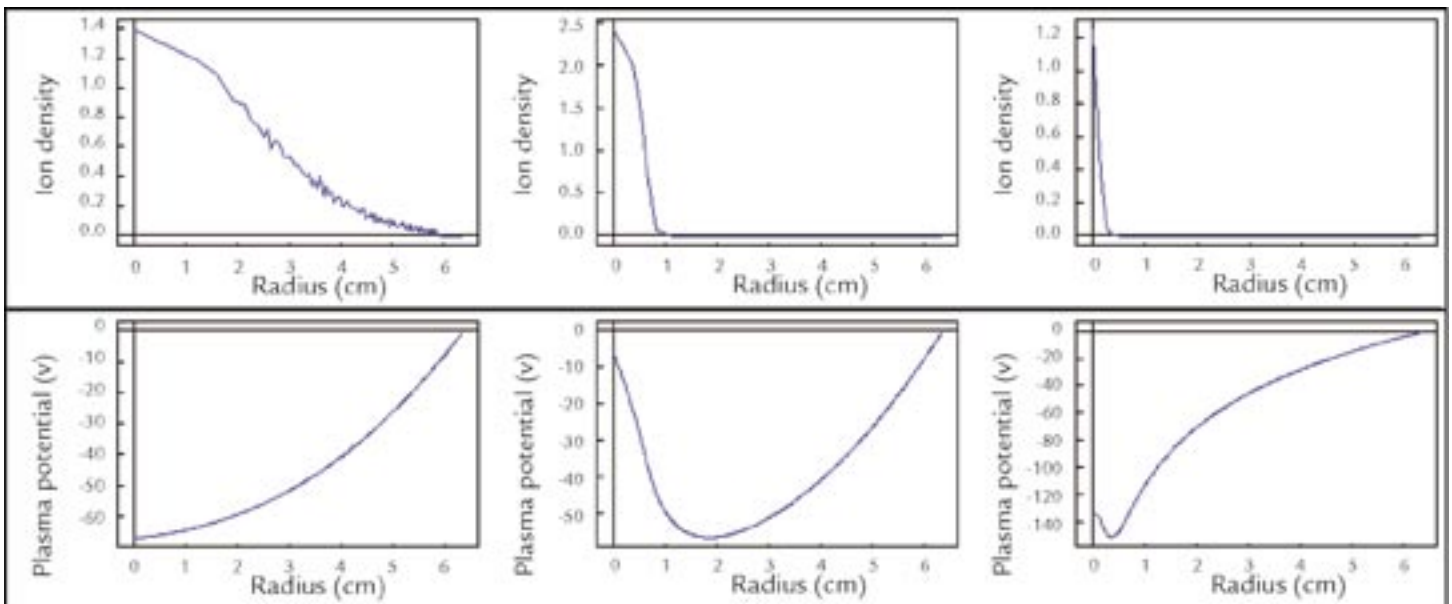
1. W.C. Elmore, J.L. Tuck, and K.M. Watson, "On the inertial-electrostatic confinement of a plasma," *Physics of Fluids* **2**, 239 (1959).
2. P.T. Farnsworth, "Electric Discharge Device for Producing Interactions Between Nuclei," U.S. Patent No. 3,358,402, issued June 28, 1966, initially filed May 5, 1956, reviewed Oct. 18, 1960, filed Jan. 11, 1962.
3. R.L. Hirsch, "Experimental studies of a deep, negative, electrostatic potential well in spherical geometry," *Physics of Fluids* **11**, 2486 (1968).
4. R.A. Nebel and D.C. Barnes, "The periodically oscillating plasma sphere," *Fusion Technology* **38**, 28 (1998).
5. J. Park *et al.*, "First experimental confirmation of periodically oscillating plasma sphere (POPS) oscillation," submitted to *Physical Review Letters*.
6. J. Park *et al.*, "Experimental studies of electrostatic confinement on the INS-e device," *Physics of Plasmas* **10**, 3841–3849 (2003).
7. R.A. Nebel *et al.*, "Theoretical and experimental studies of kinetic equilibrium and stability in the virtual cathode of the intense neutron source (INS-e) device," submitted to *Physics of Plasmas*.

Acknowledgment

This work is supported by the DOE Office of Science/Fusion Energy Sciences Innovative Confinement Concepts Program. The authors gratefully acknowledge Carter Munson (P-24), Martin Taccetti (Hydrodynamics and X-ray Physics Group, P-22), Dan Barnes (Coronado Consulting), Martin Schauer (Neutron Science and Technology Group, P-23), and John Santarius (University of Wisconsin) for many invaluable discussions on this project; Dave Beddingfield (Safeguards Science and Technology, N-1) for conducting MCNP calculations; Tom Intrator (P-24) for providing us with thoriated tungsten wire; and N-1 and the Nuclear Nonproliferation Division management for providing the facility for this experiment.

For further information, contact Jaeyoung Park, 505-667-8013, jypark@lanl.gov.

Figure 5. Radial profile of ion density and plasma potential during POPS oscillation from the one-dimensional particle code. The profiles on the left (top and bottom) come from the expansion phase, whereas the profiles in the center (top and bottom) and on the right (top and bottom) come from the collapsed phase. See the main text for a detailed description.



The World's Greatest Science Protecting America

Los Alamos National Laboratory, an affirmative action/equal opportunity employer, is operated by the University of California for the U.S. Department of Energy under contract W-7405-ENG-36.



Plasma-Enhanced Combustion of Propane using a Silent Discharge

L.A. Rosocha, Y. Kim, S. Stange, V. Ferreri (P-24),
D.M. Coates (P-DO), D. Platts (P-22)

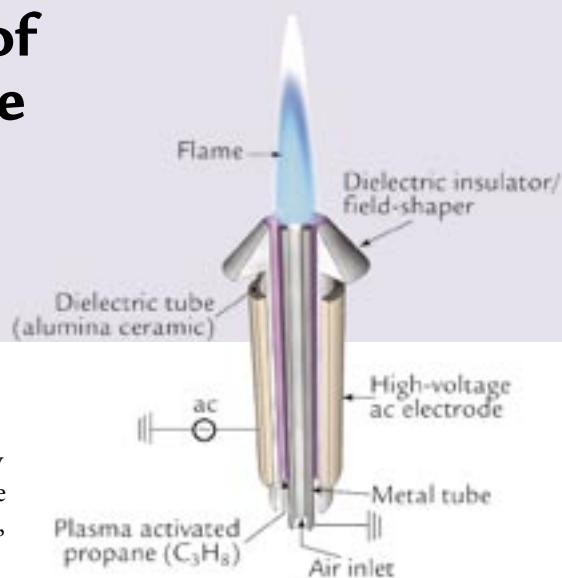


Figure 1. Schematic diagram of the experimental setup for blowout and combustion product studies, employing a coaxial DBD reactor.

As a primary objective, researchers in Physics (P) Division's Plasma Physics Group (P-24) want to minimize U.S. energy dependency on foreign resources through experiments incorporating a plasma-assisted combustion unit. Under this broad category, researchers seek to increase efficiency and reduce NO_x/SO_x and unburned hydrocarbon emissions in internal-combustion engines, gas-turbine engines, and burner units. To date, the existing lean-burn operations, consisting of a higher air-to-fuel ratio, have successfully operated in a regime where reduced NO_x/SO_x emissions are expected and have also shown increased combustion efficiency (less unburned hydrocarbon) for propane. By incorporating a lean-burn operation assisted by a nonthermal-plasma (NTP) reactor, the fracturing of hydrocarbons can result in increased power, combustion efficiency, and stability in the combustion system.

NTP units produce energetic electrons but avoid the high gas and ion temperatures involved in thermal plasmas. One NTP method, known as a silent discharge, allows free radicals to act in propagating combustion reactions, as well as intermediaries in hydrocarbon fracturing. Using NTP units, researchers have developed a fuel activation/conversion system that can decrease pollutants while increasing fuel efficiency, thus providing a path toward future U.S. energy independence.

Background

Combustion processes impact many aspects of modern life. They provide propulsion for automobiles, aircraft, and ships; generate electricity; and heat homes, water, and commercial buildings. Maximizing the efficiency of these combustion processes to conserve fuel and reduce pollution is of vital importance.

Over the past five decades, many attempts have been made to improve combustion using an electric field, which can affect flame stability, flame propagation speed, and combustion chemistry.^{1,2} However, the magnitude of the electric field in these experiments was insufficient to generate plasma. Thermal plasmas, which are usually less efficient and selective in directing electrical energy into the promotion of chemical reactions, have been applied to combustion over the past three or more decades with some success³, in particular, to convert air-fuel mixtures (into H_2 and CO)⁴, to increase internal-combustion engine efficiency, and to reduce NO_x .

NTPs are potentially more useful tools for promoting combustion. In NTPs, the electrons are energetic ("hot"), whereas ions and neutral gases are near ambient temperature ("cool"), which results

in little waste enthalpy (heat) being deposited in a process gas stream. Typical electron temperatures in such plasmas are at about a few electron volts, which is sufficient to break down the fuel and to produce free radicals.⁵ We consider the silent electric discharge⁶, also known as a dielectric barrier discharge (DBD), as a very promising candidate for combustion enhancement. In 1983, Inomata *et al.*⁷ demonstrated increases in flame speed when a DBD is applied upstream of a methane-air flame. More recent work performed by Cha *et al.*⁸ showed that applying a DBD to the flame region results in a decrease in flame length and reduced soot formation.

Our new technology, based on NTPs, pretreats fuels (not fuel-air mixtures) just before combustion.⁹ In our technique, fuels are broken down (cracked) into smaller molecular fragments, boosted

RESEARCH HIGHLIGHT

PHYSICS DIVISION

into reactive excited states, or made into “free-radicals.” The “activated” fuel is then mixed with air and combusted. This technology allows for very “lean-burn” modes of combustion highly desirable for reduction of NO_x . “Proof of principle” has been demonstrated in experiments using propane as the fuel in a flame-based burner. We investigated the effects of the plasma on combustion by examining combustion stability under lean-burn conditions, observing increases in flame propagation speed by photography, and sampling and analyzing the gas residues from combustion.

Hypothesis for NTP Combustion Enhancement

Conventional propane-air combustion begins with spark ignition, whereby a spark thermally decomposes the propane-air mixture to produce free radicals and other reactive species. Burning then continues by the propagation of the reactive species generated by the heat of combustion. The overall combustion reaction rate is usually determined by how efficiently new reactive species are generated in the propagating flame front. However, the self-generation of reactive species is sometimes insufficient to sustain combustion under certain conditions, for example, during lean-burn operation.

NTP “activation” can be used to continuously convert atomized-liquid or gaseous fuels into reactive species, so that

combustion does not rely on the self-generation of reactive species. The main possible mechanisms for fuel-cracking and fuel-activation (creation of more reactive species) are based on electron-impact processes, such as dissociation, dissociative ionization, vibrational excitation, and electronic excitation of the parent fuel molecule. Under an electron impact, propane is also ionized into multiple species, and these species then further fragment into smaller molecular ions.

Experimental Setup

We used two different NTP/DBD reactors for our investigations: one for lean-burn operation and exhaust-gas species determination and a second for flame-propagation observations. A schematic diagram of the first experimental setup⁹ is shown in Figure 1. Air flows through a grounded tubular inner electrode (diameter of 0.96 cm). Propane (C_3H_8) flows through the annular gap between the inner electrode and an alumina ceramic tube (inner diameter of 1.9 cm). The ceramic tube is surrounded by a cylindrical metal outer electrode, which is powered by a high-voltage alternating-current transformer operated at about 450 Hz to match our propane DBD reactor. An NTP was formed in the propane stream, thus activating the fuel. The inner electrode is shorter than the ceramic tube, so there is a region (of variable length, but generally < 14 mm) where the fuel and air partially mix before being ignited. A ceramic nose-cone shapes the electric field at the end of the reactor to prevent arcing.

We used the reactor shown in Figure 2 for our flame-velocity observations.¹⁰ In this experiment, the outer, high-voltage electrode was a piece of copper mesh. The mesh surrounded a quartz tube with an inner diameter of 12.5 mm. The inner electrode was a grounded stainless-steel tube having an outer diameter of 9.5 mm. Propane flowed in the annular region between the inner electrode and the quartz tube, while the air flowed down the center

of the inner electrode. The ends of the electrodes and the end of the quartz tube were separated by a 6 cm mixing region. By using a relatively long mixing region, we were able to eliminate any effects of the electric field on the flame. The air- and propane-flow rates were set to 4.6 and 0.3 lpm, respectively, to fix the equivalence ratio at 1. At an equivalence ratio of 1, combustion is stoichiometric, or ideal, so the propane should be entirely consumed.

The power deposited into the plasma was measured using Lissajous diagram techniques (charge-voltage plot).¹¹ Other diagnostics included two thermocouples to measure inlet and outlet gas temperatures, a digital camera to take photographs of the flame, and a residual-gas analyzer (RGA) equipped with a quadrupole mass spectrometer to measure the partial pressures of combustion by-products.

Experimental Results

Influence of Plasma on Flame Blowout Limits. We conducted blowout tests by holding the propane flow constant and increasing the air-flow rate until the flame blew out.¹² The blowout air-flow rate is an indicator of flame stability, and a high-blowout air-flow rate shows that combustion continues to occur under lean-burning conditions. Figure 3 shows the minimum blowout air-flow rates of an inverse, partially premixed flame for propane-flow rates between 0.2 and 0.8 lpm. The number associated with each data point in the plot corresponds to the equivalence ratio ϕ ¹³,

$$\phi = \frac{15.6 \times (\text{propane flow rate})}{(\text{air flow rate})}, \quad (1)$$

which is a standard measurement of combustion. In the absence of a plasma, the blowout limit of a propane flame increases with the propane-flow rate and begins to saturate at a propane-flow rate of 0.6 lpm. When 10 W discharge power is applied to the fuel, the blowout limit shows a large increase for low propane flow (and low equivalence ratio). However,

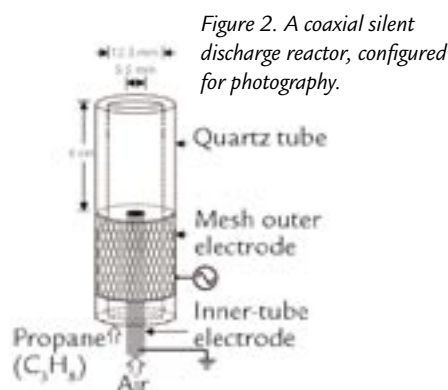


Figure 2. A coaxial silent discharge reactor, configured for photography.

the plasma benefit decreases as the propane flow increases, and for propane flow > 0.6 lpm, the blowout rate actually decreases in the presence of a plasma. This is not necessarily detrimental because low-equivalence-ratio systems show large decreases in pollutant production, especially NO_x , and are of great practical interest. In this experiment, the discharge power was held constant (10 W) while the propane-flow rate was increased. Thus, the discharge energy density ϵ ,

$$\epsilon = \frac{\text{discharge power}}{\text{gas flow rate}}, \quad (2)$$

deposited into the propane decreased as the propane-flow rate increased. For example, at a propane-flow rate of 0.3 lpm, the discharge energy density was equal to 2 kJ/L, whereas at a propane-flow rate of 0.8 lpm, the discharge energy density fell to 0.75 kJ/L. Thus, the magnitude of the discharge energy density seems to affect the blowout limit of a propane flame. More experiments will be performed to correlate the combustion enhancement with the discharge energy density.

Combustion By-products. The concentrations of gaseous products of combustion were measured with the RGA. Mass fragments of particular interest are atomic masses 26 (C_2H_2), 27 (C_2H_3), 39 (C_3H_3), and 43 (C_3H_7). During operation, the flame was ignited and allowed to burn without plasma for two minutes. Then the power supply was turned on, and the activated fuel burned for two minutes. This procedure was repeated several times to test the repeatability of any enhanced combustion provided by the plasma.

Figure 4 shows typical data (with one mass fragment, $M = 43$ shown).¹² The partial pressure of the propane fragments decrease while water and carbon dioxide (both common hydrocarbon combustion products) increase when the plasma is turned on. The plateaus at the end of the traces are the result of extinguishing the flame—these are the partial pressures in the absence of any combustion. It is clear that the plasma significantly decreases

the partial pressure of unburned hydrocarbons, indicating that propane is being burned more completely.

Flame Propagation

Speed. The photographs displayed in Figure 5 were taken with a Canon PowerShot S45 digital camera with ISO 400, a focal length of 17.5 mm, an aperture of f/8.0, and a shutter speed of 0.8 s.¹⁰ The images focus on the propane-air mixing region—the end of the quartz tube is visible at fiducial (1), and the purple glow at fiducial (2) is the edge of the outer electrode.

The progressively higher-power propane plasma's effect on the flame is shown in Figure 5. Figure 5(a) shows a propane-air flame in the absence of plasma. The application of even a relatively low-power 4 W plasma, as shown in Figure 5(b), improves the flame symmetry, a marker of stability. In both 5(a) and 5(b), the flame propagates upward only, although at an equivalence ratio of 1, it can theoretically propagate downward.¹⁴ The latter indicates that the flame propagation rate is insufficient to overcome the upward flow of the propane-air mixture. When a 6 W propane plasma is created, as shown in Figure 5(c), the flame begins to propagate downward. As larger fields are applied to the propane gas, creating higher-power plasmas, downward propagation becomes increasingly pronounced, as shown in Figures 5(d)–(f). The changes in the flame's ability to propagate downward suggest that the flame-propagation rate increases with plasma power.

The flame propagates more quickly because it is igniting and burning faster. This combustion enhancement may result from the improved cracking of propane, the creation of reactive radicals, or

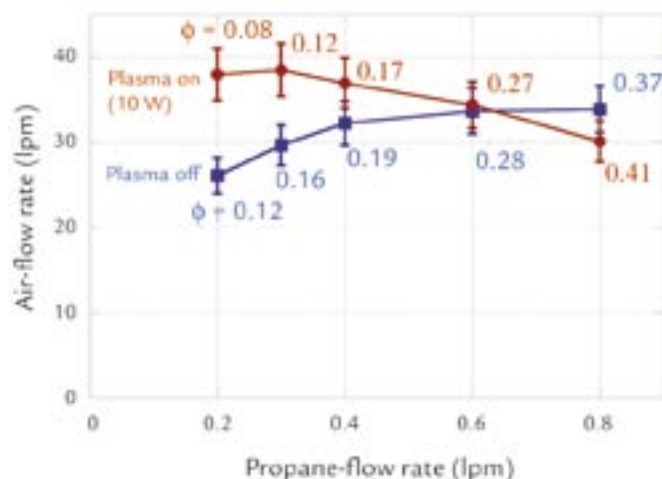


Figure 3. Effect of plasma on the blowout air-flow rate for propane flame. Combustion enhancement is indicated by the increment of the blowout limit when the plasma is on.

hydrogen generation. As discussed above, all of these factors likely play a role in combustion enhancement, but the relative importance of each is unknown. In the near future, we plan to use mixing regions of varying lengths to better understand the role of reactive radicals.

Conclusion

We have shown that silent-electrical-discharge-generated NTP can be used to activate propane fuel, significantly enhancing combustion in an activated propane-air mixture, as determined by mass spectrometric measurements of combustion-effluent gas concentrations. The plasma energy density required to achieve such enhancement is modest, of order 100s of J/L. Also, visual observations of activated propane-air flames indicate an increased spatial stability of the flame, increased blowout limits (leaner burn), and increased flame propagation speed. If applications to other fuels (e.g., gasoline, diesel, jet fuel) are successful, NTP-assisted combustion may prove to be highly beneficial to the energy needs of modern society.

References

1. J. Lawton and F.J. Weinberg, *Electrical Aspects of Combustion* (Clarendon, Oxford, 1969).
2. H.C. Jagers and A. von Engel, "The effect of electric fields on the burning velocity of various flames," *Combustion and Flame* **16**, 275–285 (1971).
3. F.J. Weinberg, Ed., *Advanced Combustion Methods* (Academic Press, London, 1986).
4. L. Bromberg *et al.*, "Emissions reductions using hydrogen from plasmatron fuel converters," *International Journal of Hydrogen Energy* **26**, 1115–1121 (2001).
5. L.A. Rosocha, "Processing of hazardous chemicals using silent electrical discharge plasmas," in *Environmental Aspects in Plasma Science*, W. Manheimer, L.E. Sugiyama, and T.H. Stix, Eds., (American Institute of Physics Press, Woodbury, New York, 1997).

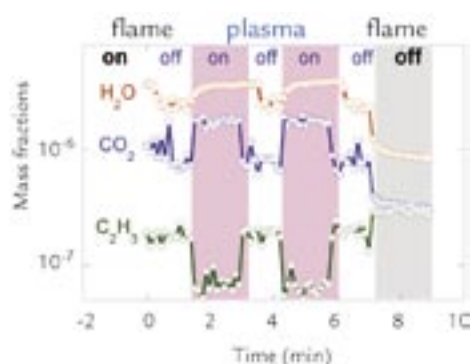


Figure 4. Mass spectrometer data for propane combustion fragments. Combustion enhancement is indicated by the reductions in unburned hydrocarbon and increases in water and carbon dioxide when the plasma is on.



Figure 5. Increasing the plasma power causes an increase in flame propagation speed, indicated by the movement of the flame towards the electrodes. Figure (a) shows combustion without a plasma. The other images show the effect of plasmas having powers of (b) 4 W, (c) 6 W, (d) 8 W, (e) 10 W, and (f) 12 W. The numbers indicate regions of interest of the apparatus: (1) is the top of the quartz tube and (2) is the top of the outer electrode. The mixing region lies between them.

6. U. Kogelschatz, "Dielectric-barrier discharges: Their history, discharge physics, and industrial applications," *Plasma Chemistry and Plasma Processing* **23**, 1–46 (2003).
7. T. Inomata *et al.*, "The application of silent electric discharges to propagating flames," *Combustion and Flame* **50**, 361–363 (1983).
8. M.S. Cha *et al.*, "Interaction between a non-thermal plasma and a flame," in *Proceedings of the 30th International Conference Plasma Science*, Cheju, Korea, June 2–5, 2003.
9. L.A. Rosocha *et al.*, "Plasma-enhanced combustion of propane using a silent discharge," *Physics of Plasmas* **11**, 2950–2956 (2004).
10. S. Stange *et al.*, "Flame images indicating combustion enhancement by dielectric barrier discharges," in *IEEE Transactions on Plasma Science* (to be published, February 2005).
11. T.C. Manley, "The electrical characteristics of the ozonator discharge," *Transactions of the Electrochemical Society* **84**, 83–95 (1943).
12. Y. Kim, S. Stange, and L.A. Rosocha, "Combustion enhancement of propane by dielectric barrier discharges," in *Proceedings of the 4th International Symposium on Non-Thermal Plasma Technology for Pollution Control and Sustainable Energy Development*, (Panama City Beach, Florida, May 10–14, 2004) pp. 221–225.
13. N.O. Nylund and A. Lawson, *Exhaust Emissions from Natural Gas Vehicles* (International Association for Natural Gas Vehicles, Sigma Group, Takapuna, New Zealand, 2000).
14. A.G. Gaydon and H.G. Wolfhard, *Flames: Their Structure, Radiation, and Temperature* (Chapman and Hall, London, 1970).

Acknowledgment

The authors wish to express their appreciation to Margaret Harris and Andrew Jensen (student interns) for technical assistance with this work and to P Division and Technology Transfer Division for financial support for this project.

For further information, contact Louis Rosocha, 505-667-8493, rosocha@lanl.gov.

Angular Momentum Transport and Dynamo Studies in the Flowing Magnetized Plasma Experiment

Z. Wang, S.C. Hsu, C.W. Barnes (P-24), K. Noguchi (T-CNLS, now Rice University), D.C. Barnes, H. Li (X-1), X.Z. Tang (T-15), S.A. Colgate (T-6)

Angular momentum transport and dynamo effects are two plasma physics problems that bear on fundamental unsolved astrophysical mysteries. Understanding angular momentum transport in weakly magnetized plasmas is important in determining, for example, the details of how galaxies form and evolve starting from nebulous clouds of matter. A solution to the dynamo problem will tell us how magnetic fields in the galaxy are created and amplified. Researchers in Physics Division's P-24 Plasma Physics Group have developed a laboratory plasma experiment to investigate these two plasma physics problems.

The problem of angular momentum transport is critical for understanding the rate at which matter collapses gravitationally to form compact objects, such as black holes, in the universe. If this happens too quickly, there will be far too many black holes in the universe; however, if this happens too slowly, then galaxies and stars and planets would never form. Because angular momentum conservation is a robust principle in physics, gravitationally collapsing globs of matter tend to become spinning disks in order to conserve their initial angular momentum. These "accretion disks" are ubiquitous in the universe and exist in the centers of galaxies (Figure 1), around binary star systems, and are an evolutionary step in the formation of solar systems. For matter to "accrete" or fall inward toward the gravitational center of a system, the angular momentum must be transported away via friction within the accretion disk plasma. However, for decades the rate at

which matter spiraled inward for many accretion disk systems was a mystery because of the inconsistency between the amount of friction thought to exist and the observationally inferred rates of accretion. The rate of interparticle collisions in disks generally cannot account for the necessary frictional forces. However, in the early

1990s, Balbus and Hawley¹ realized that a weak magnetic field in an accretion disk can lead to a plasma instability, the magnetorotational instability (MRI), which was first discovered in the 1950s. This instability could create magnetic turbulence, which can lead to the necessary frictional forces needed for the mass

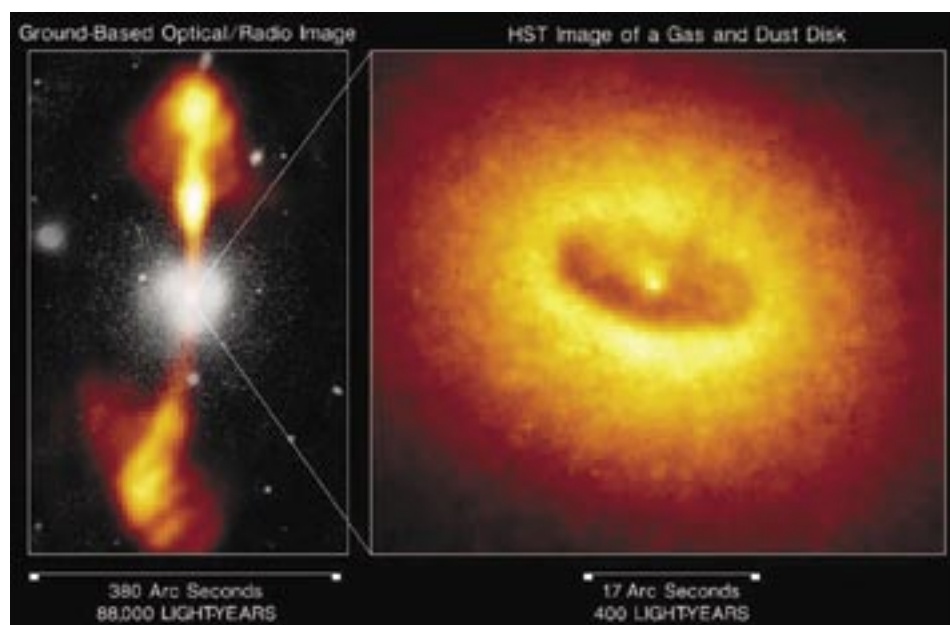


Figure 1. (a) Ground-based composite optical/radio view of elliptical galaxy NGC4261 with opposed jets emanating from galactic nucleus. (b) Hubble Space Telescope image of the core of NGC4261, showing a giant disk of cold gas and dust fueling a possible black hole. The dark, dusty disk represents a cold outer region that extends inwards to an ultrahot accretion disk within a few hundred million miles of the suspected black hole. (Credits: National Radio Astronomy Observatory, Caltech; Walter Jaffe/Leiden Observatory; Holland Ford/JHU/STScI; and NASA)

RESEARCH HIGHLIGHT
PHYSICS DIVISION

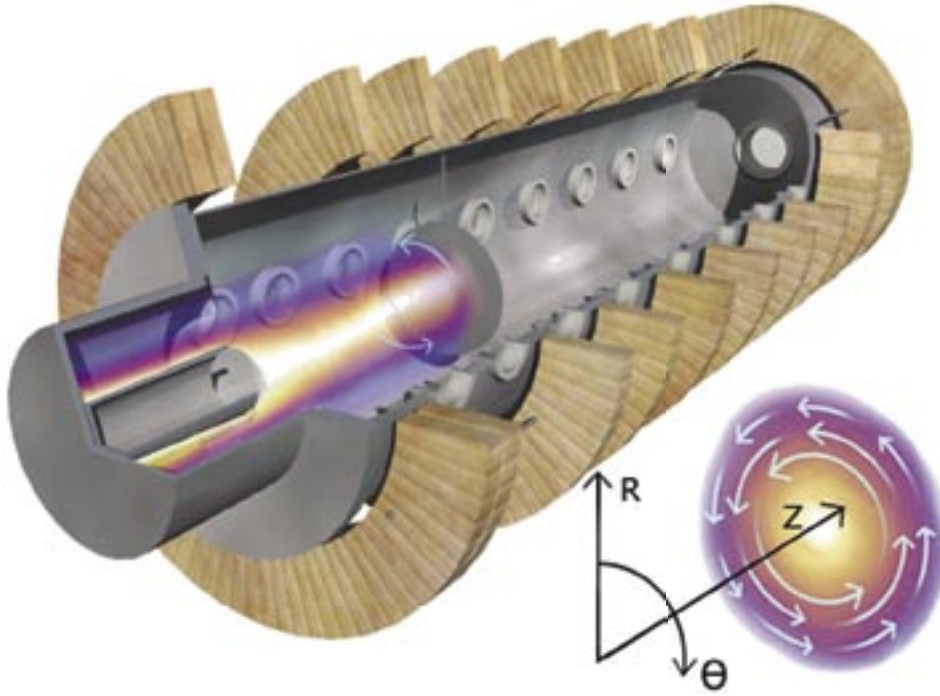


Figure 2. The FMP experimental setup consists of a coaxial plasma gun (front, left) mounted on one end of a large, cylindrical metal vacuum chamber surrounded by magnetic coils. The circular plate inside the chamber can be biased to different voltages, providing axial plasma confinement and some control over the potential profiles inside the plasma, which affects the azimuthal plasma rotation profile. A cylindrical coordinate system is used.

in an accretion disk to fall towards the central object. Over the past decade, much theoretical and computational research has advanced our understanding of the MRI and its ability to lead to increased friction in rotating disks of plasma. However, this instability has not been observed yet in plasma experiments, providing a strong motivation for this work.

The dynamo problem is another astrophysical holy grail: how are magnetic fields created and amplified on galactic scales to their observed values? Many kinds of dynamos exist, but the kind we are concerned with here involves conversion of kinetic energy in plasma flows to magnetic field energy via electrical currents created by the flowing plasma.² This process is thought to occur in galactic accretion disks, which can be thought of as magnetic engines that fill intergalactic space with magnetic energy. Again, much theoretical and numerical simulation

research has been done on the dynamo problem in recent decades, with very little experimental verification and tests. Recently, however, dynamo action was observed in a liquid-metal experiment.³ The experiments in P-24 will try to create dynamo action in a plasma experiment for the first time.

Experimental Setup

In P-24's Flowing Magnetized Plasma (FMP) experiment, researchers generate a plasma using a "coaxial gun" source, which was recycled from magnetic fusion energy research at LANL in the 1980s. The coaxial gun, which consists of two concentric cylinders, is mounted on one end of a large, cylindrical metal vacuum chamber, as seen in Figure 2. Gas is injected into the unit, and a voltage of up to 1 kV is applied across the gap between the cylinders. The gas then breaks down into a plasma as electric current up to 200 kA

flows from one gun electrode through the plasma to the other electrode. The plasma flows down the long axis of the vacuum chamber and rotates azimuthally due to electromagnetic forces. By controlling the plasma density and temperature, the plasma rotation profile, and the magnetic field strength, the experiment is expected, based on numerical calculations, to operate in regimes in which both the MRI and dynamo can be observed and studied.

Experimental measurements of magnetic field, electron density and temperature, and ion-flow speeds are required to characterize the plasma configurations created by the coaxial gun and to detect the MRI and dynamo processes. Various diagnostics are installed on the vacuum chamber to make these measurements, including

- (1) edge and internal magnetic probe coils to measure all three components of the magnetic field,
- (2) a triple Langmuir probe to measure electron temperature and density and floating electric potential,
- (3) a Mach probe to measure ion-flow speed,
- (4) a charge-coupled device camera to capture movie sequences of plasma evolution as seen in visible light emission, and
- (5) a spectroscopy system to measure ion temperature and flows via Doppler broadened emission lines.

More sophisticated probe arrays are being built by summer students to provide better diagnosis capability for the experiment.

Initial Experimental Data on FMP Plasmas

The first FMP plasma was achieved in September 2003. Coaxial-gun plasmas were created using a new low-voltage technique⁴, allowing longer plasma pulse durations for a given stored energy. Our first goal—to create and characterize the necessary plasma conditions to observe the MRI—requires the establishment of a

Angular Momentum Transport and Dynamo Studies in the Flowing Magnetized Plasma Experiment

rotating plasma within a certain range of density, temperature, magnetic field, and lifetime values. These ranges of values were determined from preliminary numerical calculations of the MRI, specifically for the geometry and conditions of the FMP experiment.⁵ These calculations also predict the initial growth rate of the instability and expected modifications to the profiles of the magnetic field and plasma pressure. The FMP diagnostics should be able to detect these signatures as the plasma transitions from a stable to unstable regime with respect to the MRI.

Camera images of the plasma evolution are shown in Figure 3. The images show that a plasma is generated in the gap between the coaxial gun electrodes. Then it flows out of the coaxial gun and quickly fills up the plasma chamber. An azimuthal rotation can also be detected from the

images. Various probes, which are scanned in the radial direction, provide profile information on magnetic field strength, ion-flow speed, and electron density and temperature.

The initial experimental data suggest that we may have a quasi-steady plasma equilibrium in which high magnetic pressure at larger radii balances the thermal plasma pressure and at smaller radii balances the rotational-kinetic pressure. The large magnetic pressure at large radii is related to a plasma “diamagnetic” effect in which the axial magnetic flux in the interior is reduced from its initial value by being expelled to the edge. The net reduction is known as the excluded flux. Diamagnetic effect is measured using two large single-turn pickup coils that encircle the plasma. The coils are at different axial positions.

The result is summarized in Figure 4. We observed that the total excluded flux is maximized when the initial axial magnetic field is around 100 G. From the measured excluded flux and a magnetohydrodynamic equilibrium model, we estimate the plasma β (ratio of the total thermal energy to magnetic field energy) is between 30%–60%. We have also observed growth of the local magnetic field (Figure 5), which will be investigated further in terms of both the MRI and dynamo.

Present experimental runs are now dedicated to characterizing the radial profiles of magnetic field, ion flow, and electron density and temperature more completely. This characterization will also be done for a variety of bias schemes on an internal bias plate in hopes of achieving the most desirable profiles for observing the MRI.

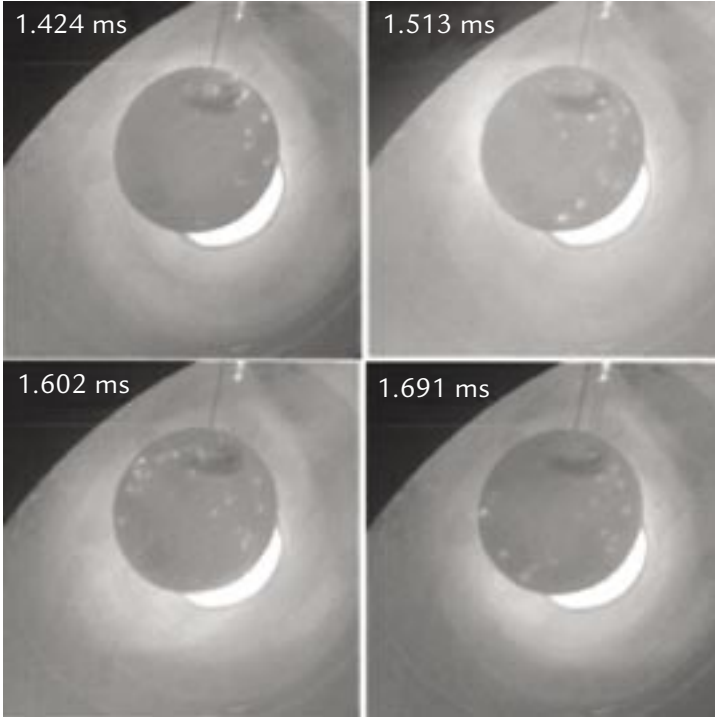


Figure 3. Evolution of an FMP plasma with a floating electrode (the black circle at center) located 1.5 m away from the coaxial gun (the brightest arc-shaped region corresponds to the coaxial gap between the coaxial electrodes). Volume light emission, as well as the bright spots on the floating electrode, appears to rotate from frame to frame. The vacuum axial magnetic field is 340 G; rotation frequency is 9.40 kHz (from magnetic probe measurements), which is slightly less than the interframe frequency of 11.2 kHz.

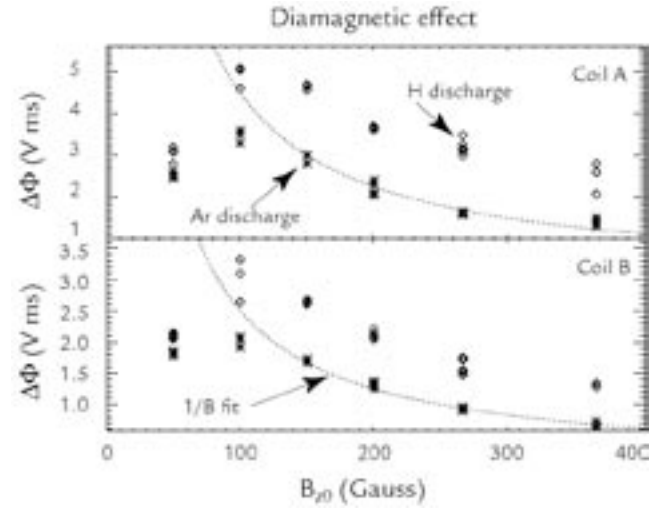


Figure 4. FMP plasma is globally diamagnetic. Axial magnetic flux (excluded flux) changes with initial axial magnetic field, which is verified at two axial (z) locations, and is labeled as Coil A for the top panel and Coil B for the bottom panel. In both panels, results for both argon (Ar, ●) gas and hydrogen (H, ○) gas are shown. The excluded flux is maximal when the initial axial magnetic field is about 100 G. The corresponding plasma (β) is between 30%–60%. The discrepancy in excluded flux between hydrogen and argon is likely due to their mass difference, which will be further studied experimentally.

Plasma Physics Research Highlights

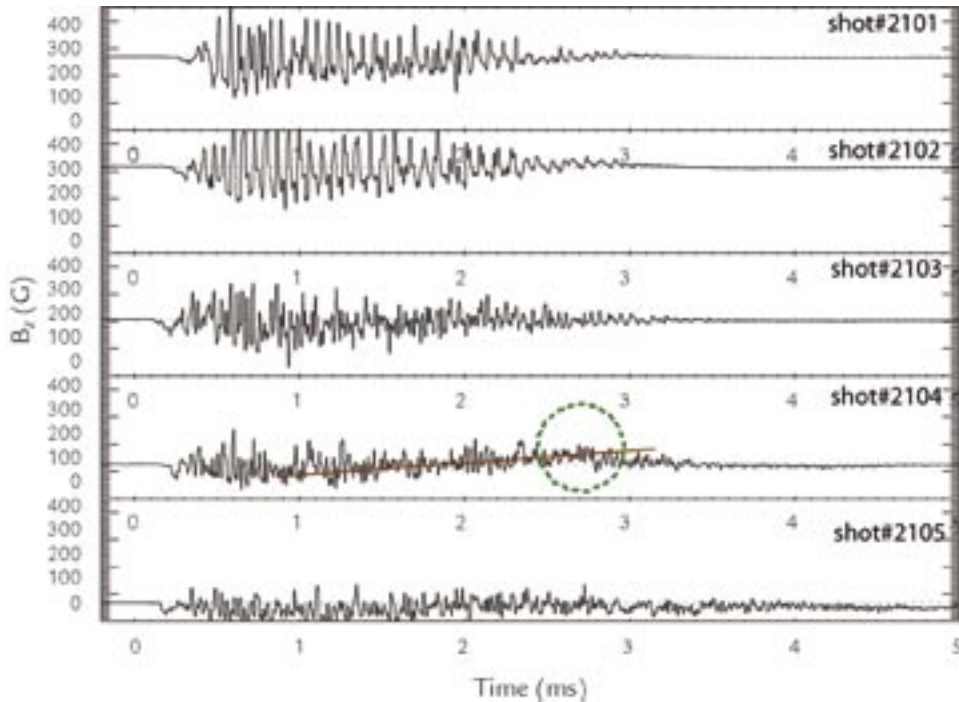


Figure 5. Study of local axial-magnetic-field (B_z) evolution under different vacuum axial-magnetic-fields ranging from 60 G to 320 G for the same coaxial-gun conditions using hydrogen plasmas. It appears that local B_z can grow on the millisecond time scale. Several mechanisms, including MRI and dynamo in high- β plasmas, are considered as candidates to explain this new observation.

Future Work

We plan to deduce the viscous damping term in the plasma force equation by measuring all of the other terms in the equation. This deduced viscosity will be compared to the theoretical value of viscosity based simply on Coulomb collisions between plasma particles. If the MRI is active, then we should expect that the experimentally deduced value for viscosity is higher than the classical value. Both MRI and dynamo will be studied by controlling flow profiles.

References

1. S.A. Balbus and J.F. Hawley, "Instability, turbulence, and enhanced transport in accretion disks," *Reviews of Modern Physics* **70**, 1–53 (1998).
2. Z. Wang *et al.*, "Laminar plasma dynamos," *Physics of Plasmas* **9**, 1491–1494 (2002).
3. A. Gailitis *et al.*, "Detection of a flow induced magnetic field eigenmode in the Riga Dynamo Facility," *Physical Review Letters* **84**, 4365–4368 (2000).
4. Z. Wang *et al.*, "A Penning-assisted sub-kilovolt coaxial plasma source," submitted to *Journal of Applied Physics* (2004).
5. K. Noguchi and V.I. Pariev, "Magnetorotational instability in a Couette flow of plasma," in *American Institute of Physics Conference Proceedings* **692**, 285–292 (2003).

Acknowledgment

This work is supported by Laboratory-Directed Research and Development/Exploratory Research funding.

For further information, contact Zhehui Wang, 505-665-5353, zwang@lanl.gov.



The World's Greatest Science Protecting America

Los Alamos National Laboratory, an affirmative action/equal opportunity employer, is operated by the University of California for the U.S. Department of Energy under contract W-7405-ENG-36.

